

UNIVERSIDADE DE SÃO PAULO
INSTITUTO DE FÍSICA DE SÃO CARLOS

AGIDE GIMENEZ MARASSI

Nuclear magnetic resonance methodologies applied for seed evaluation

São Carlos

2021

AGIDE GIMENEZ MARASSI

Nuclear magnetic resonance methodologies applied for seed evaluation

Thesis presented to the Graduate Program in Physics at the Instituto de Física de São Carlos, Universidade de São Paulo to obtain the degree of Doctor of Science.

Concentration area: Applied Physics
Advisor: Prof. Dr. Alberto Tannús
Co-Advisor: Prof. Dr. Francisco Guilhien Gomes Junior

Original Version

São Carlos

2021

I AUTHORIZE THE REPRODUCTION AND DISSEMINATION OF TOTAL OR PARTIAL COPIES OF THIS DOCUMENT, BY CONVENTIONAL OR ELECTRONIC MEDIA FOR STUDY OR RESEARCH PURPOSE, SINCE IT IS REFERENCED.

Marassi, Agide

Nuclear magnetic resonance methodologies applied for seed evaluation / Agide Marassi; advisor Alberto Tannús; co-advisor Francisco Guilhien Gomes Junior -- São Carlos 2021.

97 p.

Thesis (Doctorate - Graduate Program in Applied Physics) -- Instituto de Física de São Carlos, Universidade de São Paulo - Brasil , 2021.

1. Magnetic resonance imaging. 2. Image analysis. 3. Seed technology. I. Tannús, Alberto, advisor. II. Guilhien Gomes Junior, Francisco, co-advisor. III. Title.

FOLHA DE APROVAÇÃO

Agide Gimenez Marassi

Tese apresentada ao Instituto de Física de São Carlos da Universidade de São Paulo para obtenção do título de Doutor em Ciências. Área de Concentração: Física Aplicada.

Aprovado(a) em: 24/05/2021

Comissão Julgadora

Dr(a). Alberto Tannús

Instituição: (IFSC/USP)

Dr(a). Francisco Guilhien Gomes Junior

Instituição: (ESALQ/USP)

Dr(a). Carlos Ernesto Garrido Salmon

Instituição: (FFCLRP/USP)

Dr(a). Luiz Alberto Colnago

Instituição: (EMBRAPA/São Carlos)

Dr(a). Tais de Moraes Falleiro Suassuna

Instituição: (EMBRAPA/Santo Antonio de Goiás)

To my grandparents (*in memoriam*)
João Gimenez Lopes and Felicio Marassi

ACKNOWLEDGEMENTS

I would like to thank my academic advisor, Dr. Alberto Tannús, at São Carlos Institute of Physics, to whom I am very honored and grateful for giving me the opportunity to join the Center of Magnetic Resonance Imaging and In Vivo Spectroscopy (CIERMag) in 2013.

I also wish to thank my academic co-advisor, Dr. Francisco Guilhien Gomes Junior, at Department of Crop Science of the “Luiz de Queiroz” College of Agriculture, for bringing me all the seeds knowledge and the motivation always inspired in all our conversations.

My deepest thanks go to Dr. Bernd Uwe Foerster, for all your know-how transfer in Magnetic Resonance Imaging, for his provocations that led me to think in a more complex way and, for helping me with the implementation of the Magnetization Transfer Zero Echo Time (MT-ZTE) sequence.

I wish to thank Dr. Éverton Lucas de Oliveira, at High-Resolution NMR Laboratory of São Carlos Institute of Physics, to helping me to analysis, elaboration and provided of the graphs for relaxometry studies.

Many thanks to my friends at CIERMag, from whom I will omit the names for fear of not remembering everyone, I met fantastic people here.

Many thanks to Renata for companionship, patient and laughs during this time. I do not know how to thank you enough for helping me stay focused.

Many thanks to my parents, Valéria and Carlos and, my grandparents Madalena and Maria Ana, for all the moral support and encouragement to give me confidence to come so far.

Thanks to the funding agencies for supporting the research developed in Brazil.

*“Not only is the Universe stranger than we think,
it is stranger than we can think”*

Werner Karl Heisenberg (1901-1976)

ABSTRACT

MARASSI, A. G. **Nuclear magnetic resonance methodologies applied for seed evaluation**. 2021. 97 p. Thesis (Doctor in Science) - Instituto de Física de São Carlos, Universidade de São Paulo, São Carlos, 2021.

Damages to seeds, whether due to the occurrence of mechanical injuries, attacks by insect pests, or by pathogens, cause effects that can be evidenced after their occurrence or during storage, resulting in losses of germination and vigor. The application of the X-Ray scanning has been recommended by different associations of seed analysis as a fast and non-destructive method for seed inspection, but this technique presents limitations when assessing the depth of damage in the internal tissues of the seeds or when the density variation of the tissues is small. However, the introduction of the Nuclear Magnetic Resonance (NMR) methodologies based on the nuclear density weighted can bring advances in the study of seed quality originated on internal anatomical changes. The objectives of this research were to evaluate soybean and corn seeds by comparing X-Ray and Magnetic Resonance Imaging (MRI) between healthy, immature seeds, and those attacked by pest insects, as well as evaluating soybean seeds of high and low vigor by NMR relaxometry. Soybean and corn seeds of the same cultivar with the problems described were selected and submitted to image analysis by X-Ray and MRI with the Fast Low-Angle Shot (FLASH) and Zero Echo Time (ZTE) sequences, respectively. On the other hand, soybean of the same cultivar but with high and low vigor were selected and submitted to the relaxometry T_1 - T_2 correlation experiment. The NMR methodology allowed the identification of damage to internal seed tissues in a satisfactory way in the image, highlighting the full extent of the damage, as well as it was possible to evaluate high and low vigor seeds with this approach. Also, a new modification in the ZTE sequence was proposed. The results obtained corroborate the NMR technique as a powerful auxiliary tool in the evaluation of internal tissues and for the selection of high-quality seeds.

Keywords: Magnetic resonance image. Image analysis. Seed technology.

RESUMO

MARASSI, A. G. **Metodologias de ressonância magnética nuclear aplicadas para avaliação de sementes**. 2021. 97 p. Tese (Doutorado em Ciências) - Instituto de Física de São Carlos, Universidade de São Paulo, São Carlos, 2021.

Os danos em sementes, quer sejam pela ocorrência de injúrias mecânicas, ataques por insetos praga, ou por patógenos, acarretam efeitos que podem ser evidenciados após sua ocorrência ou durante o armazenamento, resultando na perda de vigor e germinação. A aplicação da radiografia tem sido recomendada por diferentes associações de análise de sementes como um método rápido e não destrutivo para a inspeção de sementes, mas esta técnica apresenta limitações ao avaliar a profundidade dos danos nos tecidos internos das sementes ou quando a variação da densidade dos tecidos é pequena. Entretanto, a introdução das metodologias de Ressonância Magnética Nuclear (RMN) baseadas na densidade nuclear pode trazer avanços no estudo da qualidade de sementes originado nas alterações anatômicas internas. Os objetivos desta pesquisa foram avaliar sementes de soja e milho por meio da comparação de imagens de Raios-X e Ressonância Magnética (IRM) entre sementes saudáveis, imaturas e atacadas por insetos praga, bem como avaliar sementes de soja de alto e baixo vigor por relaxometria. Sementes de soja e milho da mesma cultivar com os problemas descritos foram selecionadas e submetidas à análise de imagens por Raios-X e Ressonância Magnética com as sequências Fast Low-Angle Shot (FLASH e Zero Echo Time (ZTE), respectivamente. Por outro lado, soja da mesma cultivar, mas com alto e baixo vigor, foram selecionadas e submetidas ao experimento de relaxometria por correlação de T_1 - T_2 . A metodologia de RMN permitiu a identificação de danos em tecidos internos das sementes de forma satisfatória na imagem, destacando toda a extensão do dano, bem como foi possível avaliar sementes de alto e baixo vigor com esta abordagem. Além disso, uma nova modificação na sequência ZTE foi proposta. Os resultados obtidos corroboram a técnica de RMN como uma poderosa ferramenta auxiliar na avaliação de tecidos internos e na seleção de sementes de alta qualidade.

Palavras-chave: Imagem por ressonância magnética. Análise de imagem. Tecnologia de sementes.

LIST OF FIGURES

Figure 1 – Representation of the permanent magnetic moment μ of the atomic nuclei. The excess of charge makes the nucleus like a small magnet.	30
Figure 2 – Representation of the energetic states of a spin system without (left) and with (right) the presence of an applied external magnetic field.	31
Figure 3 – Nuclear precession movement of the nucleus in the presence of an external magnetic field.....	33
Figure 4 – Representation of a macroscopic magnetization. M_L and M_T are components vector in the directions parallel and perpendicular of the external magnetic field, respectively.	34
Figure 5 – Representation of the excitation field as a superposition of two circularly polarized counter-rotating fields in the plane perpendicular to B_0 , each of amplitude B_1	36
Figure 6 – Behavior of the magnetization vector in a rotating frame of reference in a resonant condition due the RF pulse.	37
Figure 7 – Special cases for a maximum excitation or $\pi/2$ pulse (left) and an inversion or π pulse (right).....	38
Figure 8 – A Free Induction Decay (FID) signal observed after the application of an excitation pulse. It is an oscillating signal with decreasing amplitude in time.	39
Figure 9 – Representation of a dipole-dipole interaction of a couple of spins in the presence of an external magnetic field.	40
Figure 10 – Illustration of the experiment that leads to the observation of the phenomenon known as Spin Echo.	43
Figure 11 – Example of the frequency encoding in one dimension due the application of a linear field gradient. A) Three tubes with different quantities of water. B) FID signal from individual tubes. C) Composite signal and its unidimensional Fourier transformation.	44
Figure 12 – Schematic condition for good resolution in images by MR, where the distances between the pixels center needs to be larger than its average width.....	47
Figure 13 – Schematic representation of the variation of the main magnetic field by applying a magnetic field gradient in each direction of the space. Note that each gradient encoding just one specific direction.....	49
Figure 14 – Examples of trajectories to be used in MRI to fill the k-space matrix. The figure with red arrows represents the cartesian model. The purple arrows represent the radial model. The green arrow represents the spiral model. And the blue arrow represents the zig-zag model.	51
Figure 15 – Pulse program of the 3-dimensional Fast Low-Angle Shot (FLASH) sequence. Note the encoding of the slice and phase gradients before the echo acquisition. Due the absence of the 180° pulse the echo is formed by the inversion of the polarity of the readout gradient. The major change here was the use of a Hermitian pulse, that reduced the echo time significantly.....	52

Figure 16 – Pulse program diagram of the Zero Echo Time sequence. The parameter TE reflect the impossibility to switch the transmit-receive with no time consumption, that calls the dead time. In the sequence, all the events occur when the gradients are turned on. 56

Figure 17 – Pulse program diagram of the modified Zero Echo Time (ZTE) sequence with the application of the Magnetization Transfer (MT) preparation in the form of a Gaussian pulse..... 57

Figure 18 – A cross-sectional view of a soybean (left) and a corn (right) seed. Note the small structures that are constituent elements of the embryonic axis or the embryo in these seeds. This is the most important part of a seed that will results in a new seedling and the propagation of species. 60

Figure 19 – The solenoid coil used to acquire the Magnetic Resonance Images. Two variable capacitors were placed to manually adjusted the tuning and matching when the coil and sample are placed into the magnetic field. 64

Figure 20 – Time diagram of the Transverse Relaxation Exchange (TREx) sequence. Basically, it consists of the application of two Carr-Purcell-Meiboom-Gill (CPMG) with a phase modulation in the second excitation pulse and echo acquisition. The summed of subtraction of the two data set results in T_2 - T_2 exchange or T_1 - T_2 correlation. 65

Figure 21 – Image of the Smith Chart (yellow line) that provides the complex impedance and logarithmic scale (blue line) of the measurement of the reflection parameter S11 at the frequency of 85.2 MHz captured by the Network Analyzer..... 68

Figure 22 – Image of the spherical phantom with 7 mm of diameter filled with a solution of water with copper sulfate at a concentration of 1 g/l. 69

Figure 23 – A corn seed image acquired with the FLASH sequence (left) and with the ZTE sequence (right). 71

Figure 24 – A soybean seed image acquired with the ZTE sequence (left) and with the FLASH sequence (right). 72

Figure 25 – A standard X-Ray image (A) of a healthy soybean seed compared to MRI image (B, C and, D). The MRI image was acquired with 8 averages, resulting in a 3 hours and 28 minutes of acquisition time..... 73

Figure 26 – A standard X-Ray image (A) of a soybean seed damaged by chinch bug bites compared to MRI image (B, C and, D). The MRI image was acquired with 8 averages, resulting in a 3 hours and 28 minutes of acquisition time. 75

Figure 27 – A standard X-Ray image (A) of an immature soybean seed compared to MRI image (B, C and, D). The MRI image was acquired with 8 averages, resulting in a 3 hours and 28 minutes of acquisition time..... 76

Figure 28 – A standard X-Ray image (A) and the MRI image (B, C and, D) of healthy corn seed. It is possible to observe a damage in the region of the endosperm above the plumule that is not observable with the X-Ray image..... 78

Figure 29 – A standard X-Ray image (A) and MRI image (B, C and, D) of corn seed with a weevil growing inside, destroying much of the internal tissues before hatching in its adult form.80

Figure 30 – A corn seed without (left) and with (right) the application of the Magnetization Transfer (MT). Note the reduction of the signal that comes from the region of the starch due the

saturation by the off-resonant pulse, and the presence of the signal that comes from the aleurone layer of the seed. 82

Figure 31 – The same slice of a soybean seed without (left) and with (right) the application of the Magnetization Transfer (MT) before run the ZTE sequence without hydration. The image has only two averages with acquisition time of 34 minutes and 35 seconds. 84

Figure 32 – Relaxation time curves for both T₂ and T₁ obtained by Inverse Laplace Transformation (ILT) for a single seed with high vigor during 6 hours of hydration. The dark blue curve represents the seed in storage condition. 86

Figure 33 – Relaxation time curves for both T₂ and T₁ obtained by Inverse Laplace Transformation (ILT) for a single seed with low vigor during 6 hours of hydration. The dark blue curve represents the seed in storage condition. 87

LIST OF TABLES

Table 1 – Some atomic nucleus useful for NMR that present a value of spin $\frac{1}{2}$	30
Table 2 – Reflection coefficient and values of real and imaginary part of a complex impedance acquired with a direct measurement of the solenoid coil when tuned with the frequency operation.	68
Table 3 – Quality factor of the coil with unloaded and loaded condition, and frequency displacement.	69
Table 4 – Signal-to-Noise (SNR) ratio and potency used to the application of the excitation and inversion pulses with the sequence MSME.	70

CONTENTS

1	INTRODUCTION	25
2	LITERATURE REVIEW	29
2.1	PRINCIPLES OF NUCLEAR MAGNETIC RESONANCE	29
2.1.1	ATOMIC NUCLEI AND MAGNETIC FIELDS	29
2.1.2	MACROSCOPIC EFFECTS	34
2.1.3	EXCITATION BY RADIOFREQUENCY WAVES	35
2.1.4	SPIN RESPONSE: FREE INDUCTION DECAY	38
2.1.5	THE RELAXATION MECHANISMS	39
2.2	IMAGE FORMATION	41
2.2.1	GENERAL CONCEPTS	41
2.2.2	FAST LOW-ANGLE SHOT (FLASH)	52
2.2.3	ZERO ECHO TIME (ZTE) AND MAGNETIZATION TRANSFER	54
2.3	SEED STRUCTURE AND MORPHOLOGY	58
3	MATERIALS AND METHODS	63
4	RESULTS AND DISCUSSION	67
4.1	COIL CHARACTERIZATION	67
4.2	IMAGES RESULTS	70
4.3	RELAXOMETRY RESULTS	85
5	CONCLUSIONS	89
	REFERENCES	91

1 INTRODUCTION

The challenging for conducting this research is the fact that, in addition to Brazil being a country with a strong global participation in the agricultural sector with the seed market reaching values in the order of R\$ 20 billion per year, the contribution to development new, more sophisticated seed evaluation techniques, resulting in more accurate assessment of more complex problems is a demand.¹

One of the factors that negatively affect the quality of the seeds is the mechanical damage, in some cases associated with the high moisture content, as it decreases their physical, physiological and sanitary qualities. These effects can be immediate or manifest during the storage period, resulting in the deterioration of the internal tissues of the seed or a decrease in germination and vigor.²

The physical changes are caused by expansions and contractions of the seed volume, due to fluctuations in temperature and humidity, resulting in the formation of rough walls in the cotyledons and, due to fatigue of the integument tissues, their rupture of the integument or embryonic tissues may occur.³

The physiological changes, through the deterioration process, result from an increase in the respiration rates of the seeds. As a result, there will be a decrease in mass due to the consumption of reserve material that would be used during the germination period. There will be also a breakdown of lipids and proteins, with a consequent reduction in enzyme activity.³

Some factors that influence the occurrence of these damages are the characteristics of the seeds, mainly their size, shape, thickness of the integument, type of reserve material and spatial position of the embryonic axis.⁴ Furthermore, mechanical damages result in openings in the pericarp or integument, they can result in infection points and sources of nutrients for pathogens, affecting their sanitary conditions.⁵

During the beginning of the mechanical studies on seeds, the evaluation of the occurrence of these problems was carried out with the use of contrast chemicals that, when in contact with the damage surfaces, manifested in the formation of specific stains. However, these methods have been considered obsolete, because in addition to not allowing further tests, they are not conclusive in accurately identifying the damage related to the abnormalities observed in the seedlings or with the death of the embryo.⁶

Another factor that affects the quality of the seeds is the attack by pests, especially the chinch bug bite. These insects make small holes with their stylets in the seeds, still in the pods, inject their saliva containing digestive enzymes and suck the liquefied content.⁷ The excess saliva generated solidifies, forming a sheath on the surface which can be used as an indicator of the chinch bug food activity.⁸⁻⁹

In addition, when these insects feed, they bring with them some types of yeasts,¹⁰ whose colonization results in tissue necrosis, dramatically affecting the germinative potential and the vigor of the seed.¹¹ The affected seeds may have typical stains, deformations or wrinkles, and have their chemical composition altered.¹²

Other problem that severely affect the quality of seeds is pest insect infestation, with manifestation in pre-harvest, storage and post-harvest period. Some weevil species put eggs on the surface of seeds, larvae hatch and perforation occur, to consume reserves. As it promotes an increase in temperature and humidity it favors the development of fungi and, both factors result in significant reduction of germination and seed vigor.¹³⁻¹⁴

The introduction of the X-Ray technique represented an advance in the evaluation of seed damage, first performed on corn seeds,¹⁵ and later expanded to soybean and sweet corn seeds.¹⁶⁻¹⁷ Researches results have also revealed the efficiency of radiographic analyzes in the identification of deteriorated tissues in corn seeds,¹⁸⁻¹⁹ however, the identification of these damages was only possible when the lesions are in advanced stages, making it impossible to identify them in early stages.

Despite the advances achieved by the X-Ray technique, a limitation arises in the analysis of the extent and depth of injuries or deteriorated tissues when these abnormalities are close to vital seed tissues such as the embryo. In this technique, a beam produced by an X-Ray generator is transmitted through the sample, so the different amounts of incident radiation are reflected by the sample, depending on its chemical composition and density,²⁰ therefore identifying damage to seeds in its early stages is difficulty.²¹

Recent work developed using the X-Ray computed tomography technique,²² has brought new perspectives for the analysis of seeds by image, such as, a better characterization of mechanical damage in corn seeds and their relationship with germination, as damage represents a fracture in the tissue. Even more, the

technique comes up again when damage caused by pathogens or insects causes small changes in the density of the internal tissues.

Thus, the application of more sophisticated procedures, which allow more efficient analysis of the internal conditions of seeds with greater sensitivity to small changes in tissue density, such as magnetic resonance imaging, can help in the progress of research in seed technology.

Magnetic resonance imaging has been shown to be one of the most promising imaging techniques due to its flexibility in obtaining the most varied types of contrast, as well as being a non-invasive and non-destructive technique.²³ It originates in the interaction of certain atomic nuclei when in the presence of an external magnetic field, based on the spatial encoding of the precession frequency of these nuclei, allow the visualization of internal structures with high resolution and contrast.²⁴

However, because it is a technique widely used in the clinical area, few studies are conducted on other objects of interest, resulting in an absence of knowledge and the non-use of the technique in order to explore its full potential.

The objective of this research is the development of nuclear magnetic resonance methodologies, such as image and time-domain relaxometry, to evaluate the internal tissues of seeds found in different conditions, either after the attack of insects at the time of seed formation and its manifestation, or during the storage period, as well as the evaluation of low and high vigor seeds whose differences result in changes in the germination period.

The results presented here corroborate the techniques of nuclear magnetic resonance as an auxiliary tool, along with the other techniques already established, in the evaluation of seeds. The validation of these results may contribute to the monitoring and selection of high-quality seeds.

2 LITERATURE REVIEW

In this chapter, structured in three parts, a review of the literature covered in this work is presented, first discussing the basic principles of the Nuclear Magnetic Resonance phenomenon. After that, a deeper discussion of the theory of formation of the image by Magnetic Resonance is shown. Finally, a brief discussion of the basic structures present in seeds and their morphology is presented.

2.1 PRINCIPLES OF NUCLEAR MAGNETIC RESONANCE

In this section, a review of the concepts of the theory of nuclear magnetic resonance is conducted. First, it is discussed about atomic nuclei and their behavior in the presence of an external magnetic field, the macroscopic effects of an ensemble of nuclei, as they are always found in a collective manner nor alone, the forms of prepare a magnetic resonance signal as an excitation of the spin system by pulsed radiofrequency waves and their response, and finally the mechanisms that brings the spin system to the equilibrium condition after a perturbation.

2.1.1 ATOMIC NUCLEI AND MAGNETIC FIELDS

The atomic nuclei useful for Magnetic Resonance Imaging (MRI) have a fundamental property for the occurrence of the magnetic resonance phenomena that is an intrinsic angular momentum or spin (S) and associated with a permanent magnetic moment (μ). These two quantities can be expressed as follow

$$S = \hbar m_s \quad (1)$$

$$\mu = \gamma S \quad (2)$$

where m_s is the eigenvalue of the angular momentum, \hbar is Planck's constant and γ is called the nuclear gyromagnetic ratio whose value depends on the nuclear species.²⁵ See Table 1 for some examples of nuclei that has spin $\frac{1}{2}$.

Table 1 – Some atomic nucleus useful for NMR that present a value of spin $\frac{1}{2}$.

Element	Natural Abundance (%)	γ (MHz/T)
^1H	99.98	42.58
^{13}C	1.11	10.71
^{15}N	0.37	4.31
^{19}F	100	40.05
^{31}P	100	17.23

Source: Adapted from HAACKE *et al.*²⁶

Protons, neutrons, whole nuclei, and electrons possess spin and are often represented as tiny spheres spinning about your axis (Figure 1). Therefore, spin can only be measured in discrete units, either integer or half-integer values. Hydrogen, the nucleus most commonly used for MRI has spin half ($\frac{1}{2}$), the same spin as the single proton of which it is composed. Only nuclei with non-zero spin can absorb and emit electromagnetic radiation and undergo resonance when placed in an external magnetic field.

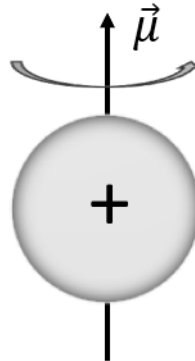


Figure 1 – Representation of the permanent magnetic moment μ of the atomic nuclei. The excess of charge makes the nucleus like a small magnet.

Source: By the author.

In the subatomic regime governed by quantum mechanics, nuclei are better understood as probability waves rather than objects. Because of the Heisenberg Uncertainty Principle, it is impossible to know the exact direction of a particle's spin at any point in time. However, it is possible to measure and know with certainty some limited value about the spin, such as a component of its angular momentum along a single direction. When a quantity is possible to be observable, it is known as an

eigenstate. The number of eigenstates for a nucleus with non-zero spin is given by the $(2s + 1)$ rule.

Hence for the hydrogen nucleus, there are two possible spin states, often referred to as spin-up and spin-down or parallel and anti-parallel respectively. In the absence of an external magnetic field, the two separate spin states for hydrogen are not observable and said to be degenerate. If an external magnetic field is applied, an interaction occurs allowing the two separate states to be measured (see Figure 2).

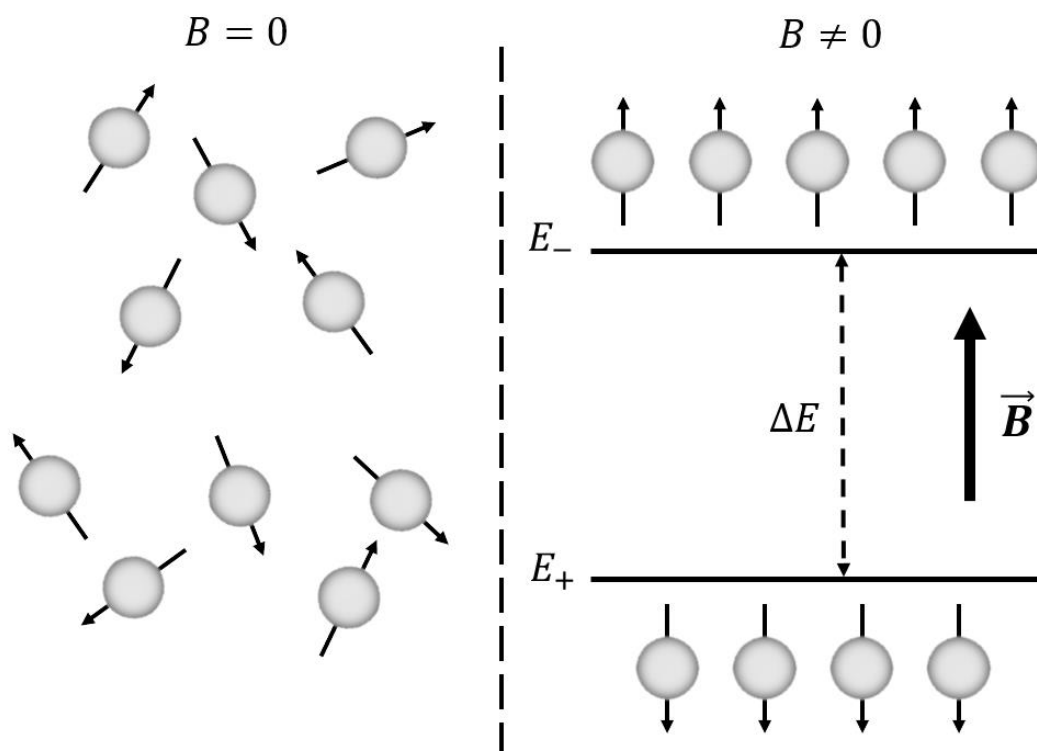


Figure 2 – Representation of the energetic states of a spin system without (left) and with (right) the presence of an applied external magnetic field.

Source: By the author.

The physical separation of both states reflects an energy difference between them and this is known as the nuclear Zeeman effect, that can be expressed by a dot product of a magnetic moment μ and the external magnetic field B , represented as the follow Hamiltonian of interaction (H):

$$H = -\mu \cdot B \quad (3)$$

In the presence of the external magnetic field the energy gap (ΔE) between two nuclear spin states scales directly with magnetic field amplitude and is given by the follow equation

$$\Delta E = \gamma \hbar B \quad (4)$$

Also, the possible states are separated by a discrete energy gap and corresponding frequency. The relationship between the change in energy of an atomic system levels by emission or absorption of a photon of frequency ω is

$$\Delta E = \hbar \omega \quad (5)$$

Thus, combining equations 4 and 5 results in

$$\omega = \gamma B \quad (6)$$

The Equation 6 is known as Larmor equation, showing that the NMR resonance frequency is simply the gyromagnetic ratio times the strength of the magnetic field. Also, due the absence of the Planck's constant a non-quantum explanation using classical physics is possible.

In a spin system at temperatures close to absolute zero, the majority of spins would have quantum amplitudes favoring the lower energy state. At room temperatures, however, this tendency for spins to prefer the lower energy level is opposed by thermal motions that tend to equalize the two energy levels. The resultant equilibrium distribution is predicted by the Boltzmann distribution:²⁷

$$N_+/N_- = \exp(-\Delta E/k_B T) \quad (7)$$

where N_+ and N_- represent the number of spins one would expect to measure in the spin-up and spin-down states, ΔE is the difference in energy between the two states, k_B is the Boltzmann constant, and T is the absolute temperature in Kelvin.

In classical theory, a rotating object possesses a property known as angular momentum. This quantity is a form of inertia, reflecting the macroscopic object's properties like size, shape, mass, and rotational velocity, and it is typically

represented as a vector pointing along the axis of rotation by the right-hand rule (represented by vector $\boldsymbol{\mu}$ in Figure 3).

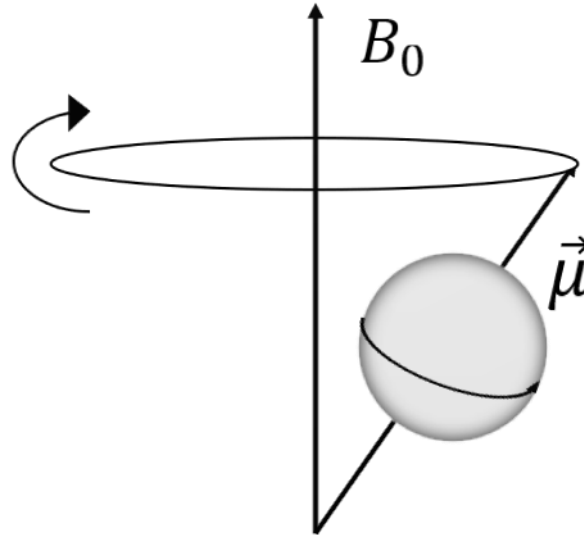


Figure 3 – Nuclear precession movement of the nucleus in the presence of an external magnetic field.

Source: By the author.

Thus, the magnetic field \mathbf{B} produces a torque, $\boldsymbol{\mu} \times \mathbf{B}$, on the magnetic dipole moment $\boldsymbol{\mu}$ of the nucleus. This torque, being normal to the angular momentum vector, continuously changes the spinning direction making the nuclear moment $\boldsymbol{\mu}$ precess around the magnetic field \mathbf{B} .²⁸ This result can be written as

$$\frac{d}{dt}\vec{\mu} = -\gamma\vec{B} \times \vec{\mu} \quad (8)$$

Assuming that the magnetic field exists only in the z direction and that the magnetic moment vector can be writing as an arbitrary vector in the space, the general expression of the magnetic moment vector could be expressed as:

$$\mu(t) = [\mu_{x0} \cos(\omega t) + \mu_{y0} \sin(\omega t)]\hat{i} + [\mu_{x0} \sin(\omega t) - \mu_{y0} \cos(\omega t)]\hat{j} + \mu_{z0}\hat{k} \quad (9)$$

which means that the component of the nuclear magnetic moment μ perpendicular to the magnetic field B precess around it with a Larmor angular frequency (Equation. 6).

2.1.2 MACROSCOPIC EFFECTS

Instead of think about the behavior of all individual spin, think to the effect of a magnetic field in an ensemble of spins like in any macroscopic sample. So, in an elementary tissue volume composed with a large number of nuclei, ideally homogeneous in composition, known as the term *voxel*, whose proton magnetization density will be related by the pixel brightness in the MRI image.

Net magnetization M is the sum of average magnetic moment μ from all spins in the sample, and at thermal equilibrium M is aligned with B . Like individual spins, M can be tipped into transverse plane and will precess around B until return to the equilibrium condition (see Figure 4).²⁹

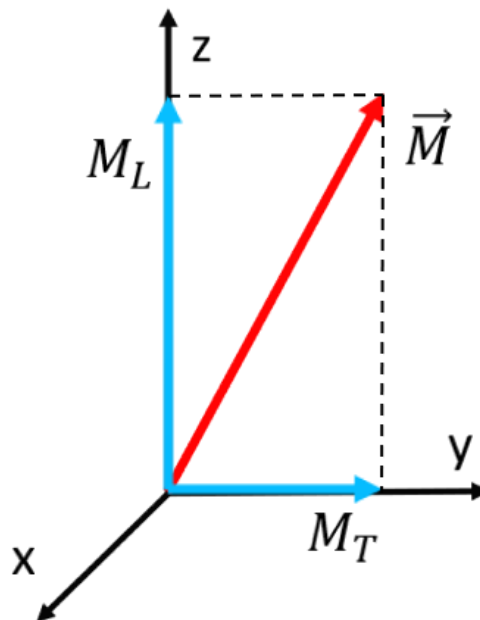


Figure 4 – Representation of a macroscopic magnetization. M_L and M_T are components vector in the directions parallel and perpendicular of the external magnetic field, respectively.

Source: By the author.

So, if no external magnetic field is present these moments will be randomly oriented and the net magnetization will be zero (Equation 10).

$$M = \sum_i \mu_i \quad (10)$$

In an applied field B , the transverse component of each moment is rotating around the field with the same frequency ω , but with random phases in thermal

equilibrium. Thus, at this condition, there is not net magnetization component transverse (M_T) to the field and

$$M_T = 0 \quad (11)$$

The component of μ in the direction of the magnetic field could be either parallel or anti-parallel to it. At temperature T , due to thermal fluctuations, both orientations are presented with a small portion appointing in the parallel lower energy direction. This results in a net equilibrium magnetization, longitudinal to the external field (M_L), given by²⁹

$$M_L = M_0 = \frac{\hbar^2 \gamma^2 B}{4k_B T} \quad (12)$$

where \hbar is the Plank's constant, γ is the nuclear gyromagnetic ratio, B is the value of the external magnetic field, k_B is the Boltzmann constant, and T is the absolute temperature.

Thus, the nuclear spin system can be excited, changing the values of M_L and M_T from those given above. Also, it is observed that these values return exponentially to their initial conditions at thermal equilibrium with time constants T_2 and T_1 , known as transversal and longitudinal relaxation times respectively.

Due the fact that the microscopic mechanisms that relax the longitudinal component of μ are also effective in relaxing the transversal component, M_T relaxes faster than M_L . In other words, T_2 is shorter than T_1 .

2.1.3 EXCITATION BY RADIOFREQUENCY WAVES

The phenomenon involved in the measurement of the magnetization is Nuclear Magnetic Resonance (NMR), that occurs when the frequency of the radiofrequency (RF) excitation is approximately the same frequency as the precession of the nuclear moments in the external magnetic field, the Larmor frequency ω_0 . The results are a resonant excitation of the nuclear system, and the subsequent observation of the response.

Suppose a generator that can apply short pulses of time τ connected to a coil where an oscillating magnetic field B_1 , perpendicular to static magnetic field B_0 is produced and dissipated at the coil. Also, the frequency ω_1 of the magnetic field B_1 is closed to the natural frequency ω_0 of the spins in the presence of the field B_0 and its magnitude is $2B_1$.³⁰

Summarizing, Figure 5 shows an example of a superposition of two circularly polarized counter-rotating fields applied in a plane normal to the static magnetic field B_0 , each of amplitude B_1 .

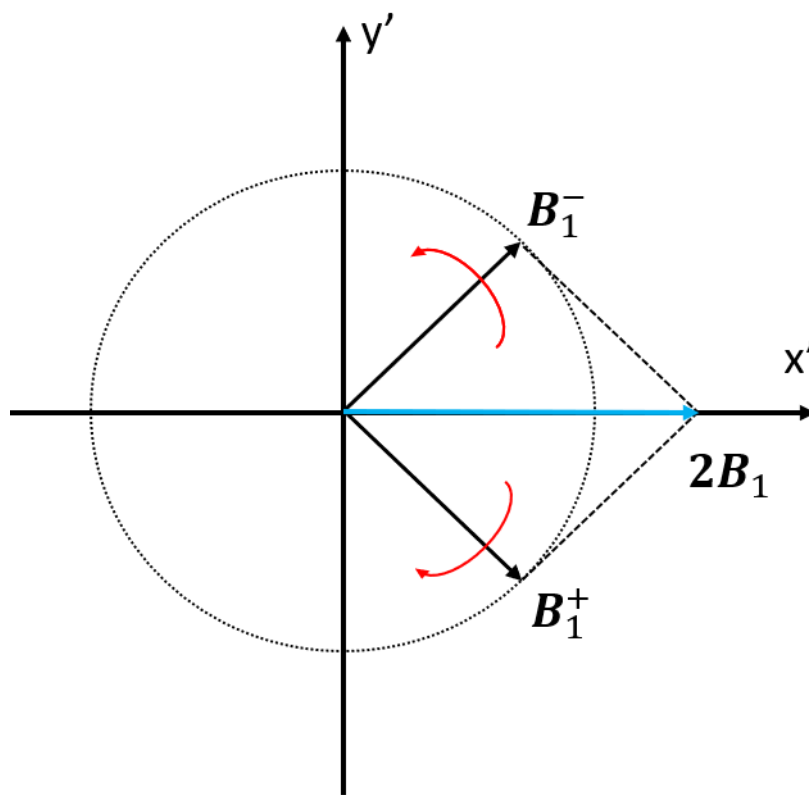


Figure 5 – Representation of the excitation field as a superposition of two circularly polarized counter-rotating fields in the plane perpendicular to B_0 , each of amplitude B_1 .

Source: By the author.

For nuclear moments precessing at Larmor frequency, one of the components will look stationary, while the other will be in the opposite direction. Ignoring this last one, that will have no first order effect, and look at the situation for a coordinate system rotating around B_0 with angular frequency ω_0 . In this frame the nuclear moments will only see a field B_1 at fixed angles to them as illustrated in Figure 6.³¹⁻³²

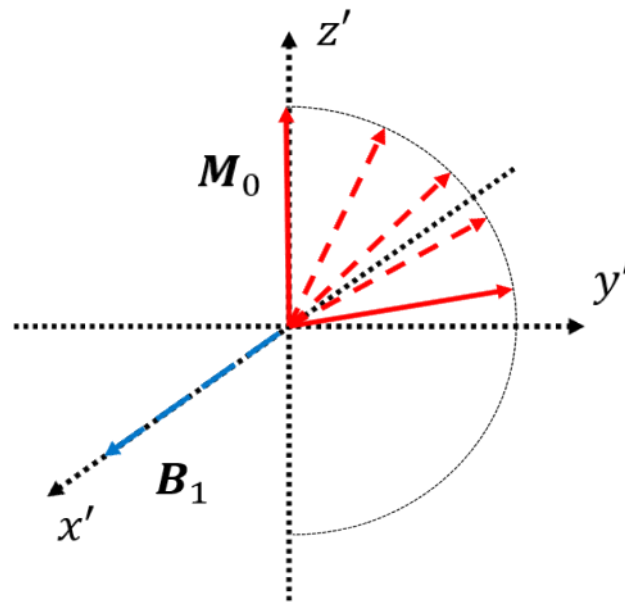


Figure 6 – Behavior of the magnetization vector in a rotating frame of reference in a resonant condition due to the RF pulse.

Source: By the author.

Now, since the total magnetization is the sum of the overall nuclear moments, it will also precess around B_1 at the same angular frequency ω_1 . So, if the RF pulse lasts τ seconds, the original equilibrium magnetization, M_0 , initially along B_0 , would have rotated around B_1 by a certain angle, described by Equation 13.³³

$$\theta(t) = \int_0^{\tau} \gamma B_1(t) dt \quad (13)$$

This implies in the creation of a non-zero transverse magnetization

$$M_T = M_0 \sin(\theta) \quad (14)$$

This is a non-equilibrium situation, associated with the increase of the internal energy of the nuclear spins system due to the resonant RF excitation. Two special cases are those for $\theta = \pi/2$ and $\theta = \pi$. RF pulses that produce this rotation are called $\pi/2$ and π pulses and are respectively used to excite and invert the magnetization (see Figure 7).³⁴

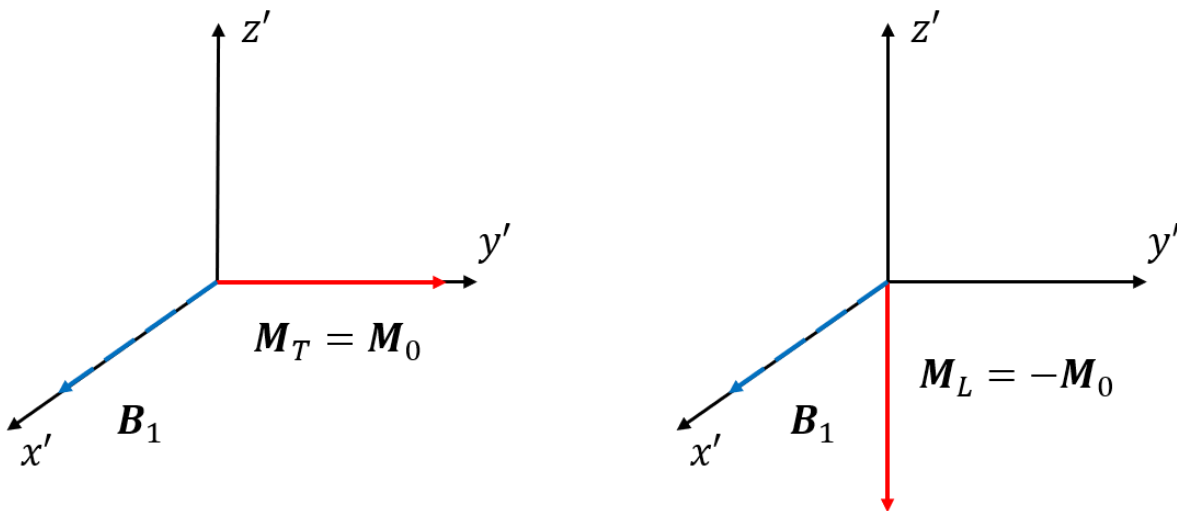


Figure 7 – Special cases for a maximum excitation or $\pi/2$ pulse (left) and an inversion or π pulse (right).

Source: By the author.

2.1.4 SPIN RESPONSE: FREE INDUCTION DECAY

Immediately following an excitation pulse ($\pi/2$ pulse), a magnetization perpendicular to B_0 and equal in size to the equilibrium value M_0 is present in all excited voxel. It will then start precession in the transverse plane at Larmor frequency ω_0 . Denoting this initial condition by $M_T(0)$ and using complex notation to represent a vector in the plane, after a time t , the following expression represent the magnetic resonance signal:

$$M_T(t) = M_T(0) \exp(i\omega_0 t) \exp(-t/T_2^*) \quad (15)$$

where the last exponential term represents the relaxation of this non-equilibrium condition, and therefore a transient transverse component, towards its thermal null value. If this signal is measured by an oscilloscopic, the behavior of it is close related to expressed in Figure 8.³⁵

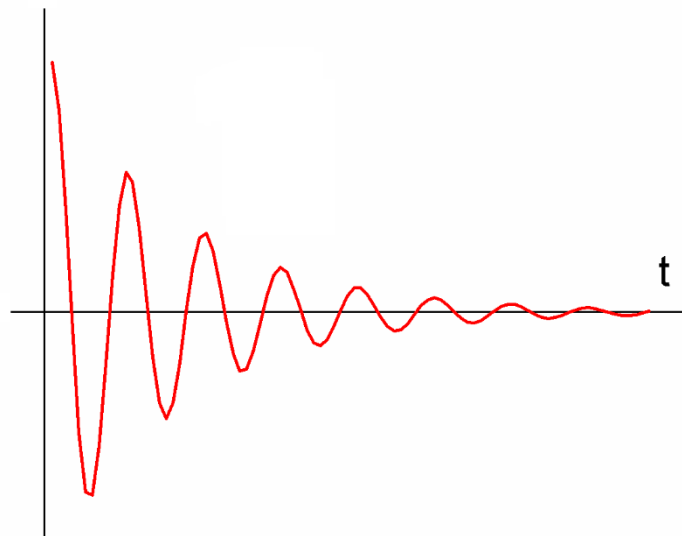


Figure 8 – A Free Induction Decay (FID) signal observed after the application of an excitation pulse. It is an oscillating signal with decreasing amplitude in time.

Source: By the author.

Each voxel of volume dv will have a moment $M_T(t)dv$ and will thus be equivalent to a small magnet that will induce in the receptor a small oscillating electromagnetic field of frequency ω_0 and decreasing amplitude. This is called the Free Induction Decay (FID) signal whose amplitude is a measure of the voxel magnetization and thus proportional to the local proton density. The overall signal from all nuclei will be the sum of those coming from the individual voxels, if all experience the same field B_0 , the one gets an FID of amplitude proportional to the total number of the selected nuclei.

2.1.5 THE RELAXATION MECHANISMS

It was discussed before that the longitudinal magnetization is a result of the excess number of individual moments precessing with its component parallel to the external magnetic field. With the same idea, in order to have a finite magnetization transverse to the field, a limited number of nuclear moments must be precessing in-phase, that is, their transverse components must be pointing in the same direction. This phasing of the spins is imposed by the RF pulse during the resonant excitation.

The return to equilibrium after an excitation pulse involves two different mechanisms that take place at the same time although at different rates: relaxation of

the transverse component, called transverse of T_2 relaxation and recuperation of the longitudinal component, called longitudinal or T_1 relaxation.

The microscopic mechanisms behind these two processes require the random fluctuation of the nuclear spin interactions. For the case of protons in tissue, the most relevant of this is the dipole-dipole interaction between the nuclear moment and its neighborhoods, resulting in the random reorientations of the tissue molecules (see Figure 9).³⁶⁻³⁸

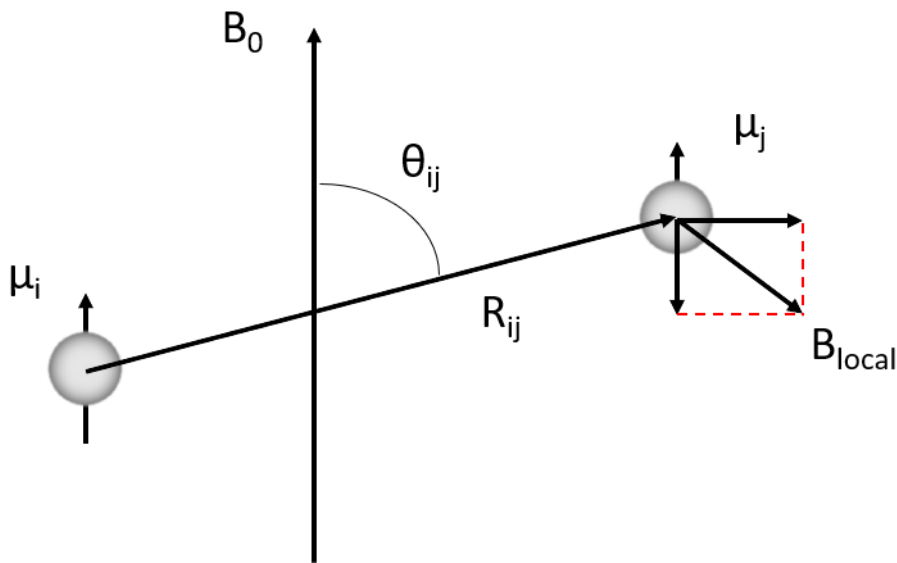


Figure 9 – Representation of a dipole-dipole interaction of a couple of spins in the presence of an external magnetic field.

Source: By the author.

For instance, consider the local field produced by a dipole μ at the site of another placed at a distance R . The module of this field is represented by the follow expression:³⁸

$$|B_{local}| = \mu \frac{(3 \cos^2 \theta - 1)}{R^3} \quad (16)$$

This local field has components perpendicular and parallel to main field B_0 and both will undergo rapid as well as slow fluctuations due to changes in angle θ with molecular motions.³⁹

Consider first the perpendicular component of the randomly time dependent field $B_{local}(t)$, some of the fast fluctuations may introduce high frequencies near ω_0 , in

its frequency spectrum. This resonant harmonic component of the perpendicular local field will produce random rotations of the local moments μ with two major effects.

First, it randomly changes the phases of the individual spins precession, destroying phase coherence between them and thus decreasing transverse magnetization, contributing to the T_2 relaxation. Second, by changing the component of the moments μ parallel to B_0 , it allows the exchange between the nuclei magnetic energy, given by the dot product of $(\mu \cdot B_0)$, and the thermally excited mechanical energy of the moving molecules. This is a thermalization process that takes the longitudinal magnetization to its equilibrium value, and it is therefore responsible for the T_1 relaxation.

Now, the component that is parallel to the external field cannot produce spin rotations, no matter its frequency spectrum, and therefore does not contribute to T_1 . On the other hand, the slow fluctuating parallel local field, adds to B_0 producing local random changes is the nuclear Larmor frequency. This makes some nuclei precess faster than others, destroying their phase coherence. This mechanism also contributes to T_2 relaxation. This is the fact why the transverse magnetization relaxes faster than the longitudinal magnetization, that is, T_2 is smaller than T_1 .

2.2 IMAGE FORMATION

In this section, divided into three subsections, a more detailed discussion of the technical concepts of image formation by magnetic resonance will be elaborated, the use of field gradients for the preparation and spatial encoding of the precession frequencies of atomic nuclei and the various possibilities of store the set of data obtained from the sample for subsequent image generation.

2.2.1 GENERAL CONCEPTS

All the discussion above assume that an external magnetic field is perfectly uniform. This is not the real case because finite real magnets do not produce perfectly homogeneous fields. Also, magnetic field gradients are used to encode the nuclear spin signals to create an image.

There is an important difference between the external magnetic field static inhomogeneity, and the real, intrinsic, due to internal magnetic fields fluctuations. In

fact, while T_2 is associated with random interactions, and therefore involves a spontaneous thermodynamically irreversible process, T_2^* results from the evolution of the spins phases under unknown but well-defined conditions, given by the intensity of the external magnetic field at the individual nuclear positions.

This makes possible the following experiment, that leads to the observation of the phenomenon known as spin echo signal with a pulse sequence $[\pi/2 - \tau - \pi]$. Connecting an oscilloscope to the receiver coil will then show the usual decaying FID signal following the excitation pulse, and an additional signal, that first grows and then decays, peaking at time 2τ . This extra signal that shows the reappearance of a transverse magnetization, after it had apparently disappeared, at a time well beyond T_2^* , was named a Spin Echo.⁴⁰

The Figure 10 shows the evolution of the spin isochromats (a group of spins that precess with the same frequency) in a rotating frame. After being phased by the $\pi/2$ pulse the various isochromats begin to precess at slightly different frequencies given by the local values of the external field. In the rotating frame the slow isochromats will be seen rotating in opposite direction compared to the fast ones. This starts the dephasing process, and the isochromats continue to fan out in this way for a time τ until the application of the π pulse. At this time every nuclear moments μ is rotated by 180° around the RF pulse. Now the difference in precession frequencies makes the isochromats to fan in at the same rate, so that the transverse magnetization is almost completely refocused τ seconds later, except for the small fraction irreversibly lost by the intrinsic T_2 relaxation.

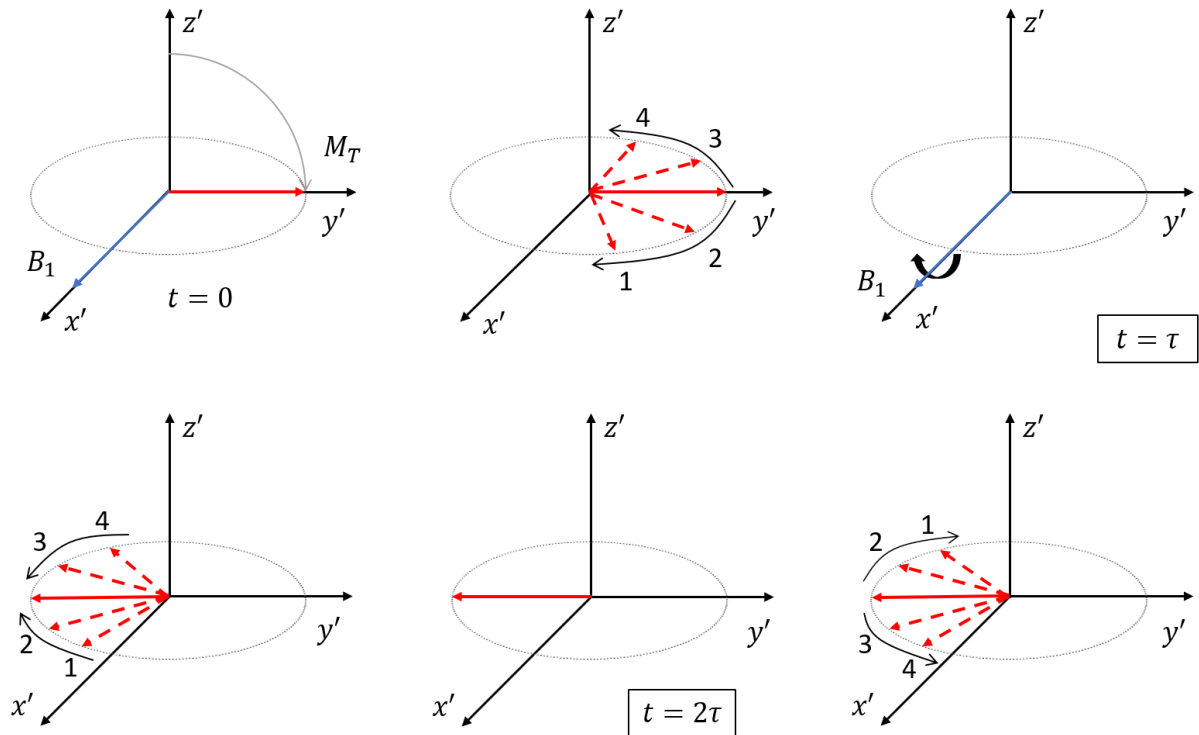


Figure 10 – Illustration of the experiment that leads to the observation of the phenomenon known as Spin Echo.

Source: Adapted from FOERSTER.⁴¹

In the presence of an external magnetic field the macroscopic magnetization $\mathbf{M}(\mathbf{r})$ is proportional to the overall proton density $\rho(\mathbf{r})$. The key procedure for the mapping of the magnetization is the spatial encoding of the nuclei position that is based on the precession frequency dependence on the magnetic field given by Larmor equation (Equation 6).

A spatially dependent magnetic field is made by superimposing to the static, homogeneous field B_0 , a linearly varying field parallel to it, with constant amplitude gradient, such as, in x direction

$$B(\mathbf{r}) = B_0 + G_x \cdot x \quad (18)$$

and consequently

$$\omega(\mathbf{r}) = \gamma(B_0 + G_x \cdot x) \quad (19)$$

with, assuming that the external magnetic is appointing in the z direction,

$$G_x = \frac{\partial B_z(\vec{r})}{\partial x} \quad (20)$$

How the spatial dependence of the frequency given above (Equation 19) is used for the mapping of the proton distribution is better understood consider the simple example below.

Three tubes filled with different amounts of water are placed at positions x_1 , x_2 and x_3 where the fields are respectively B_1 , B_2 and B_3 . After the application of the excitation pulse their magnetizations will precess with frequencies ω_1 , ω_2 and ω_3 , generating a composite signal $s(t)$ as illustrated in Figure 11.

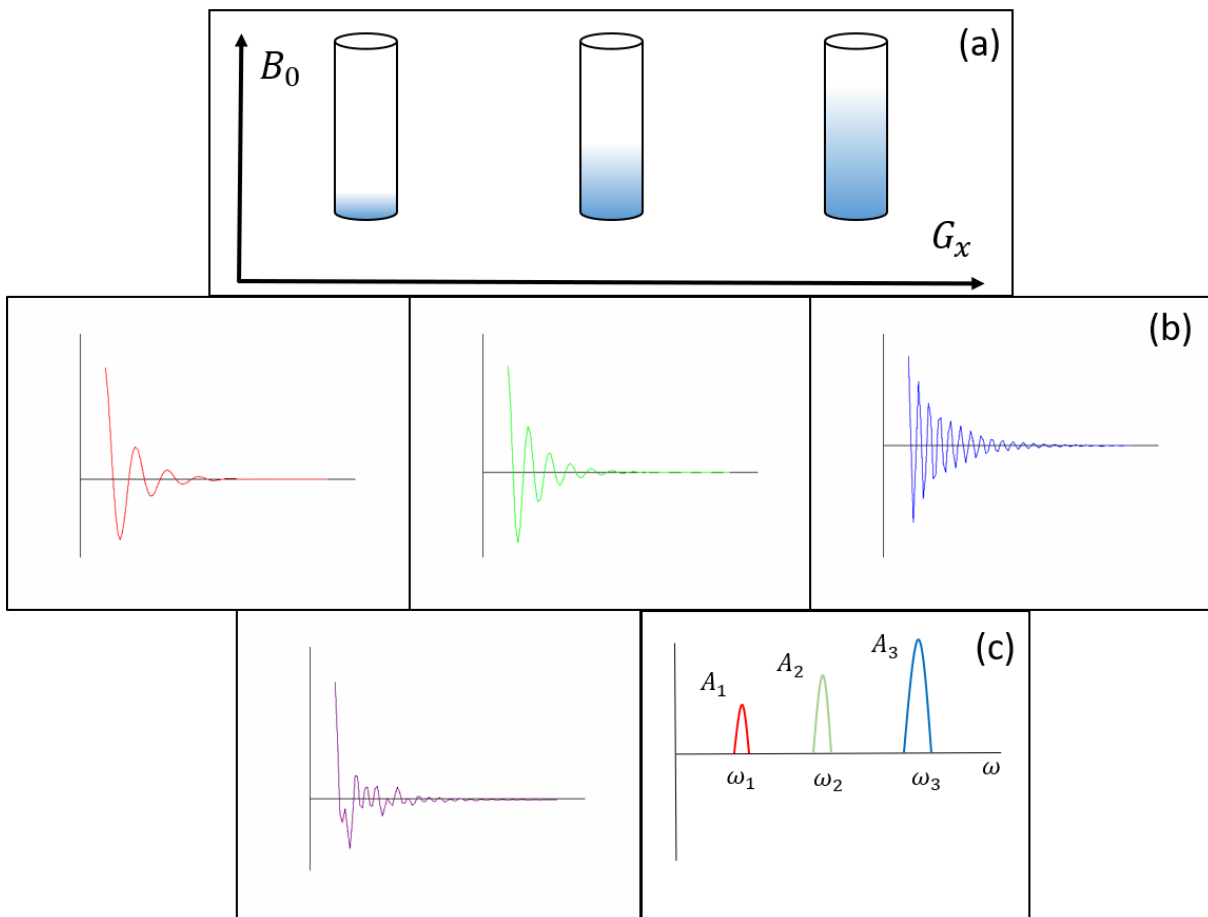


Figure 11 – Example of the frequency encoding in one dimension due the application of a linear field gradient. A) Three tubes with different quantities of water. B) FID signal from individual tubes. C) Composite signal and its unidimensional Fourier transformation.

Source: Adapted from PAIVA.⁴²

The detected signal is easily decoded using Fourier transformation formalism. The Fourier transform of $s(t)$ gives its spectral composition, that is, how much signal

is present at each frequency component. In the Figure 11-c, three peaks at frequencies ω_1 , ω_2 and ω_3 , return amplitudes A_1 , A_2 , and A_3 , respectively proportional to the number of hydrogen nuclei present in each tube. Since one knows the relation between frequency and position of the tubes, this spectrum is in fact the one-dimensional image of the object, as it tells how much water is at each position.

Now, suppose a finite linear object having an equilibrium magnetization density $\mathbf{M}(\mathbf{x})$, then, just after excitation, the transverse magnetic moment of the volume element dx localized at x is

$$dm(x, t) = M(x) \exp(i\omega(x)t) \exp(-t/T_2) dx \quad (21)$$

The resulting signal comes from the contribution of all elements, giving

$$s(t) \propto \int_x M(x) \exp(i\gamma(B_0 + G \cdot x)t) \exp(-t/T_2) dx \quad (22)$$

Due the fact that the magnetization is zero out of the object of interest, the limits of the integral can be extended to the infinity, and Equation 22 could be written as:

$$s(t) \propto \exp(i\omega_0 t) \int_{-\infty}^{+\infty} M(x) \exp(i\gamma G x t) \exp(-t/T_2) dx \quad (23)$$

This is a modulated RF signal at the Larmor frequency, where the information about the spatial spin distribution is in the envelope. Introducing the new variable $k(t) = \gamma \cdot G \cdot t$, that express the spatial frequency domain, the Equation 23 turns as:

$$s(k(t)) \propto \exp(-k(t)/\gamma G T_2) \int_{-\infty}^{+\infty} M(x) \exp(ik(t) \cdot x) dx \quad (24)$$

Ignoring the oscillating factor, the Equation 24 could be written as a product of two functions,

$$W(k(t)) = \exp(-k(t)/\gamma G T_2) \quad (25)$$

and

$$G(k(t)) = \int_{-\infty}^{+\infty} M(x) \exp(ik(t) \cdot x) dx \quad (26)$$

The last equation shows that the image, $M(x)$, is related to $G(k)$ by a Fourier transform operation. The measured signal is $s(k)$, and not $G(k)$.

Using the convolution theorem,⁴³ the Fourier transform of $s(k)$ can be written as

$$\mathcal{F}\{s(k)\} = \mathcal{F}\{W(k) \cdot G(k)\} = \mathcal{F}\{W(k)\} \otimes \mathcal{F}\{G(k)\} \quad (27)$$

or

$$\mathcal{F}\{s(k)\} = P(x) \cdot M(x) \quad (28)$$

For an exponential T_2 decay, the function $P(x)$ is given by

$$P(x) \propto (1 - (\gamma GT_2)^2 x^2)^{-1} \quad (29)$$

This is called the Point Spread Function (PSF) and is characteristic of the experiment. In this case it is a Lorentzian function of x , with half width given by:

$$\Delta x = (\gamma GT_2)^{-1} \quad (30)$$

This width gives the minimum possible size of the image points or pixels. This also limits the resolution and thus the accuracy with which the image represents the object (see Figure 12).

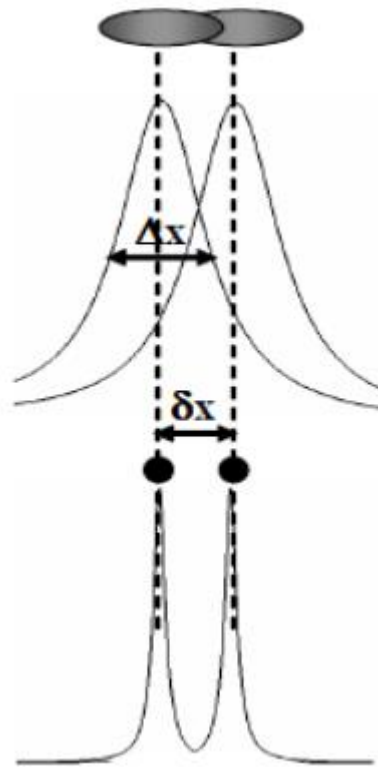


Figure 12 – Schematic condition for good resolution in images by MR, where the distances between the pixels center needs to be larger than its average width.

Source: Adapted from PAPOTI.⁴⁴

In fact, because of the properties of the Fourier transform, there is a relation between the pixel size or interpixel distance in the resulting image, δx , and the maximum spatial frequency contained in the sampled signal k_{max} . This relation is $\delta x = 1/k_{max}$, and since k was defined as γGt , the distance interpixel is expressed as:

$$\delta x = (\gamma G T_{max})^{-1} \quad (31)$$

Here appears the condition to observe an unblurred image. According to the Rayleigh criterion, two pixels are distinguishable only if their separation δx is larger than their width, Δx , that is

$$\delta x < \Delta x \quad (32)$$

or

$$\gamma G t_{max} < \gamma G T_2^* \quad (33)$$

To satisfy these conditions one can either increase the gradient strength or improve the field homogeneity to longer T_2^* . In any case the better the magnet, that is, the lengthen T_2^* , the longer is the usable $t_{max} < T_2^*$,⁴⁵ and therefore the maximum achievable resolution. When this condition is satisfied, $P(x)$ narrows to a near delta function. Then, the convolution theorem says that Equation 24 can be written approximately as

$$s(k(t)) \cong \int_x M(x) \cdot \exp(ik(t) \cdot x) dx \quad (34)$$

In these conditions the one-dimensional Image $M(x)$ is the Fourier transform of the acquired NMR signal, $s(k)$.

In more than one dimension the encoding is more complex and the reason is that the spatial frequency encoding obtained from Larmor equation in one dimension was based on the existence of a magnetic field $B(x)$, with a different value at each point of the one-dimensional object. In two or three dimensions it is impossible to have a field $B(x,y)$ with a different intensity at each point (x,y) because it must be continuous in space. The solution is to encode each dimension at a time making the main magnetic field B_0 to vary only along one direction, y , for some time and then along the other direction, x . This has two implications, first, that the field must now be a function of time and space $B_0(r,t)$, and second that, in general, the overall encoding process will involve a series of experiments to produce a two or three dimensional array of data. The solution is to allow the gradients to vary, either in amplitude or direction, making them a time varying vector function $\mathbf{G}(t)$, with components given as

$$G_x(t) = \left. \frac{\partial B_0^z}{\partial x} \right|_t, G_y(t) = \left. \frac{\partial B_0^z}{\partial y} \right|_t, G_z(t) = \left. \frac{\partial B_0^z}{\partial z} \right|_t \quad (35)$$

These gradients are generated by three specially designed coil sets that produce fields parallel to B_0 each varying along the three axes as illustrated in Figure 13.

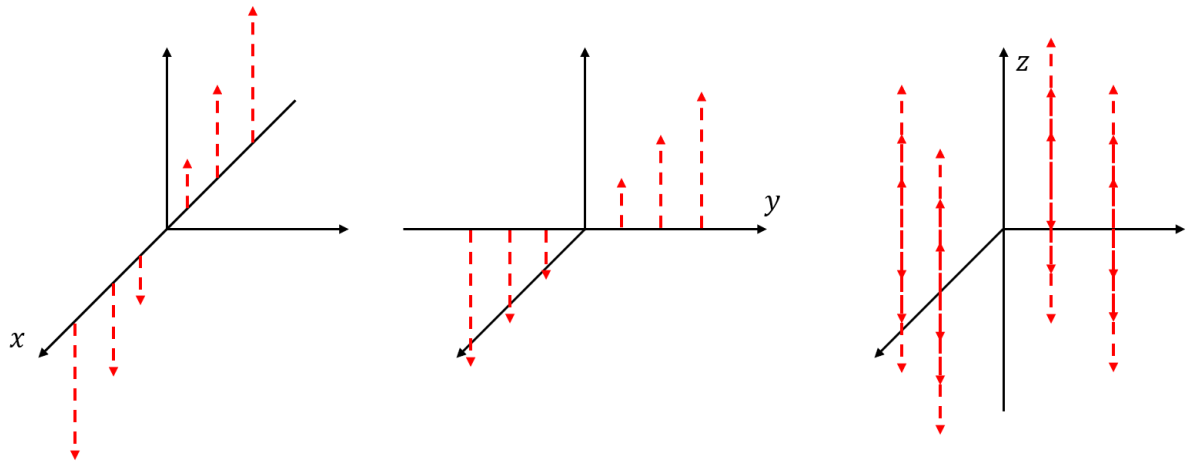


Figure 13 – Schematic representation of the variation of the main magnetic field by applying a magnetic field gradient in each direction of the space. Note that each gradient encoding just one specific direction.

Source: By the author.

Then, the magnetic field resultant by the superposition of the gradient becomes:

$$B(\vec{r}, t) = B_0 + \vec{r} \cdot \vec{G}(t) \quad (36)$$

which gives

$$\omega(\vec{r}, t) = \omega_0 + \gamma \vec{r} \cdot \vec{G}(t) \quad (37)$$

Since ω is now a function of space and time, the phase accumulated by a given voxel magnetization at a time t after excitation is given by

$$\Theta(\vec{r}, t) = \int_0^t \omega(\vec{r}, t') dt' = \omega_0 t + \vec{r} \cdot \gamma \int_0^t \vec{G}(t') dt' \quad (38)$$

and redefining k by its more general expression,

$$\vec{k}(t) = \gamma \int_0^t \vec{G}(t') dt' \quad (39)$$

Results for Equation 38, now in the rotating frame, can be expressed as

$$\theta(r, t) = \vec{r} \cdot \vec{k}(t) \quad (40)$$

which allows, similarly all steps from Equation 22 to Equation 34, to write for the demodulated signal the expression

$$s(\vec{k}(t)) \cong \int_V M(\vec{r}) \cdot \exp(i\vec{r} \cdot \vec{k}(t)) dv \quad (41)$$

For obtain an image it is necessary to know the signal, $s(\vec{k})$, over a domain in *phase space*, \vec{k} , and the maximum values of it in each direction in this *k-space* gives the resolution in the corresponding direction in *real space*.

The *k-space* is an array of numbers representing spatial frequencies in the MR image. Each number is just a data point derived directly from the MR signal. The bright intensity in the image represents the relative contribution of that point unique spatial frequency to the final Image.

The grid of k-space is commonly displayed in rectangular or cartesian array with principal axes k_x and k_y that are related to the horizontal and vertical axes of the image, respectively, but they also can be displayed in radial, spiral, and zig-zag (see Figure 14). Moreover, the individual points represent spatial frequencies in the x and y directions rather than positions, and actually they have all the information about every pixel in the final image.⁴⁶

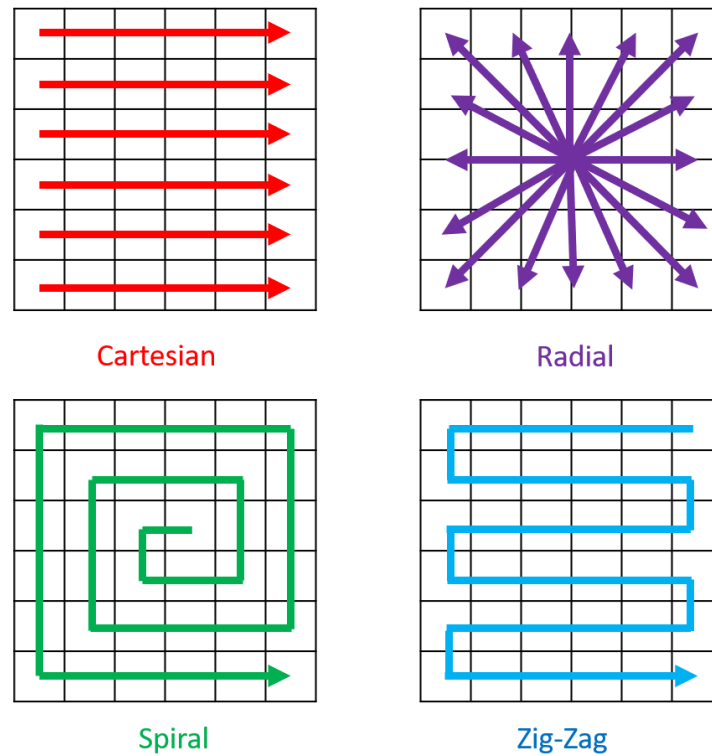


Figure 14 – Examples of trajectories to be used in MRI to fill the k-space matrix. The figure with red arrows represents the cartesian model. The purple arrows represent the radial model. The green arrow represents the spiral model. And the blue arrow represents the zig-zag model.

Source: By the author.

One advantage for this purpose is that the data elements are regularly spaced and can be placed into standard processors designed for Fast Fourier Transformation. Another property of the *k-space* is the connection between the position of data and the information about the MR image. Data next to the center of *k-space* corresponds to low special frequencies and are related to contrast of the image while data far away from the center that corresponds to high special frequencies are related to the resolution of the image.⁴⁷

Currently in radial sampling a group of several parallel lines are collected in each acquisition time, that receive the name *PROPELLER* (Periodically rotated overlapping parallel lines with enhanced reconstruction).⁴⁸ The set of acquisition are then rotated about a certain angle at which time a second set of data are acquired, and the process continues until the entire *k-space* has been collected, but at the beginning radial acquisition was made sampling individual lines each acquisition time.

One advantage of this method of data acquisition is that it allows oversampling in all directions without an extra time consumed. Furthermore, due the fact that radial acquisition occurs in all directions, oversampling in not restricted to a single axis in k-space array. But, some disadvantage can occur related to gradient delays and distortions that results in a misinformation about the location of sample in different directions of the image.⁴⁹

2.2.2 FAST LOW-ANGLE SHOT (FLASH)

The Fast Low-Angle Shot (FLASH) sequence is a general Gradient Recalled Echo (GRE) that employ a spoiler gradient on the slice select gradient channel axis during the end of the module to destroy any remaining transversal magnetization after the readout, which is the case for short repetition times. As a result of this spoiler gradient, only longitudinal magnetization remains during a subsequent sequence (see Figure 15).⁵⁰⁻⁵¹

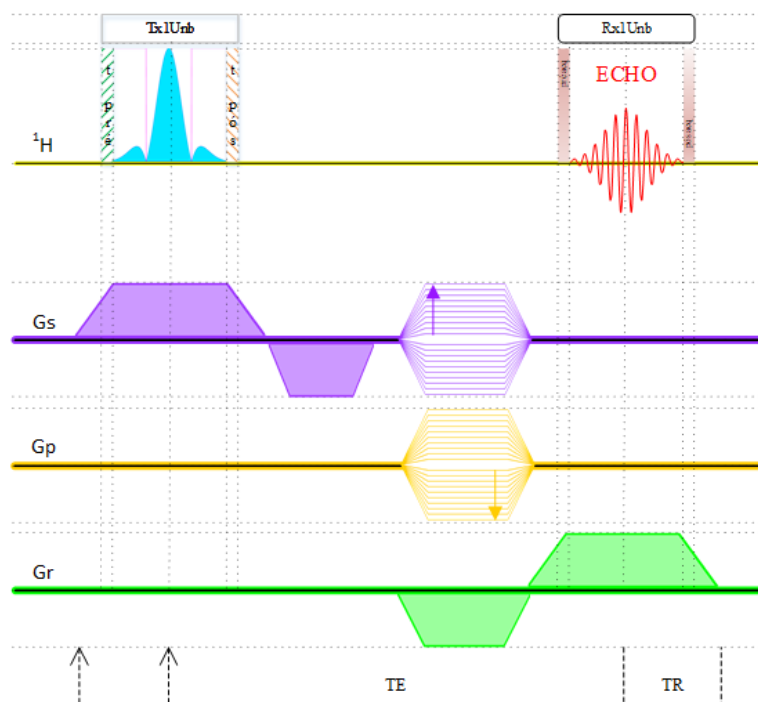


Figure 15 – Pulse program of the 3-dimensional Fast Low-Angle Shot (FLASH) sequence. Note the encoding of the slice and phase gradients before the echo acquisition. Due the absence of the 180° pulse the echo is formed by the inversion of the polarity of the readout gradient. The major change here was the use of a Hermitian pulse, that reduced the echo time significantly.

Source: By the author.

The signal intensity of a FLASH sequence is given by⁵²

$$S \propto \rho M_0 e^{-TE/T_2^*} \frac{1 - e^{-TR/T_1}}{1 - \cos(\alpha) e^{-TR/T_1}} \sin(\alpha) \quad (42)$$

where ρ is the proton density, M_0 the equilibrium magnetization, and α the flip angle. Since the TE determines the intensity of T_2^* in the FLASH image, it is preferably that TE is as short as possible.

Note that when $TE \ll T_2^*$ and large, the above expression becomes independent of T_2^* , hence the term T_1 -weighting. Assuming a good spoiling and ignoring the T_2^* effects, the signal intensity dependence on flip angle and T_1 of a FLASH sequence can be simplified as follows

$$S \propto \rho M_0 \frac{1 - e^{-TR/T_1}}{1 - \cos(\alpha) e^{-TR/T_1}} \sin(\alpha) \quad (43)$$

However, this expression does not consider the reception sensitivity factor of the coil when the same apparatus that is used for excitation is also used for reception. Therefore, the signal expression for the FLASH sequence needs to be modified to include the reception sensitivity of the coil. Assuming that the principle of reciprocity applies, the signal expression of a FLASH image is determined by⁵³

$$S \propto \rho(\kappa \cdot M_0) \frac{1 - e^{-TR/T_1}}{1 - \cos(\kappa \cdot \alpha) e^{-TR/T_1}} \sin(\kappa \cdot \alpha) \quad (44)$$

where κ is a spatially dependent sensitivity factor which modulates both the excitation flip angle and the reception sensitivity, and α is the nominal flip angle.

Since the signal in Equation 43 decreases with the flip angle for angles greater than the Ernst angle, and the receiver sensitivity that is proportional to B_1 generated by the coil depends on κ linearly, the measured signal described by Equation 44 may have an approximately constant value over a range of κ for which the flip angle is above the Ernst angle. The Ernst angle (θ_E) is calculated by the following expression

$$\cos(\theta_E) = \exp(-TR/T_1) \quad (45)$$

On the other hand, gradient echo image suffers from some artifacts that can appear but can also be avoided. The first and not always visible is a distortion of the slice profile (in 2D) especially when using large flip angle and short repetition time, due to the large flip angles in the center and low flip angles at the edges of the slice, resulting in a heavy saturation in the center and almost no saturation at the edges of the slice profile.⁵⁴

Also, all gradient echo imaging suffers from the common feature of FID signal, that is the T_2^* relaxation. The intensity of the signal depends on magnetic field inhomogeneities and chemical effects. Given a magnetic field inhomogeneity by the gradient δG within a pixel of a diameter Δr , the phase spread will appear during the echo time as follows⁵⁵

$$\phi = \gamma \cdot \delta G \cdot \Delta r \cdot TE \quad (46)$$

High values of Φ results in low intensity signal in gradient echo imaging. So, the magnetic field homogeneity effects decrease when the spatial resolution increases or the echo time decreases. This effect, known as susceptibility artifact appears in the regions near air-soft tissue interphases.

A similar effect occurs when different chemical shift values are present in the signal, with two close frequency components present, resulting in an oscillation of the signal during T_2^* decay. At some specific intervals of time, the signal appears in-phase or in out-phase. So, choosing an appropriate echo time, two images can be made by an in-phase image and an out-phase image, resulting in two different contrast images.

2.2.3 ZERO ECHO TIME (ZTE) AND MAGNETIZATION TRANSFER

The sequence named Zero Echo Time is useful for imaging of objects or tissues with very short transverse relaxation times. The MR images of samples with this behavior requires a spatial encoding and data acquisition to started and finished rapidly after the signal creation by an excitation pulse, that can be realized with radial encoding, in order to achieve both high signal-to-noise ratio and high spatial resolution.⁵⁶

Furthermore, the ZTE sequence offers others features, for instance, the gradient could never need to be switched off but only gradually changed to cover the entirely image, resulting in a reduction of noise in the acquisition. Also, minimal gradient changes reflect in the reduction of eddy currents artifacts.⁵⁷

However, the MRI scanner needs to meet two requisites to be able to perform a ZTE sequence. First, the RF pulse needs to be of high bandwidth to uniformly excite the full range of Larmor frequencies induced by the gradients. Second, the transmit-receive switching needs to be as fast as possible, but inevitably some data are lost, resulting in an initial period of dead time, due to intrinsic hardware operation. To overcome these requirements, it can be used a nonselective RF hard pulse with modern transmit-receive switch hardware, and algebraic reconstruction to recover the data lost.

A particularity in the ZTE sequence is an inherently three-dimensional method due the presence of the projection gradient, that prevents simultaneous slice selection in some specific direction. Also, due to the absence of the echo time (TE), a reduction in contrast options and an increase in susceptibility artifacts caused by extremely short-lived MR signals can occur.⁵⁸

Figure 16 shows a traditional sequence known as ZTE. Both events of radiofrequency pulse and acquisition window occurs when all gradients are turned on. The events 't-pre' and 't-pos' in hydrogen channel for both RF and acquisition window are related to the finite time hardware switching. In addition, the parameter 'delay' reflects the dead time as discussed early, and also that it is necessary to wait a certain time for dissipate the RF power deposited in the coil.

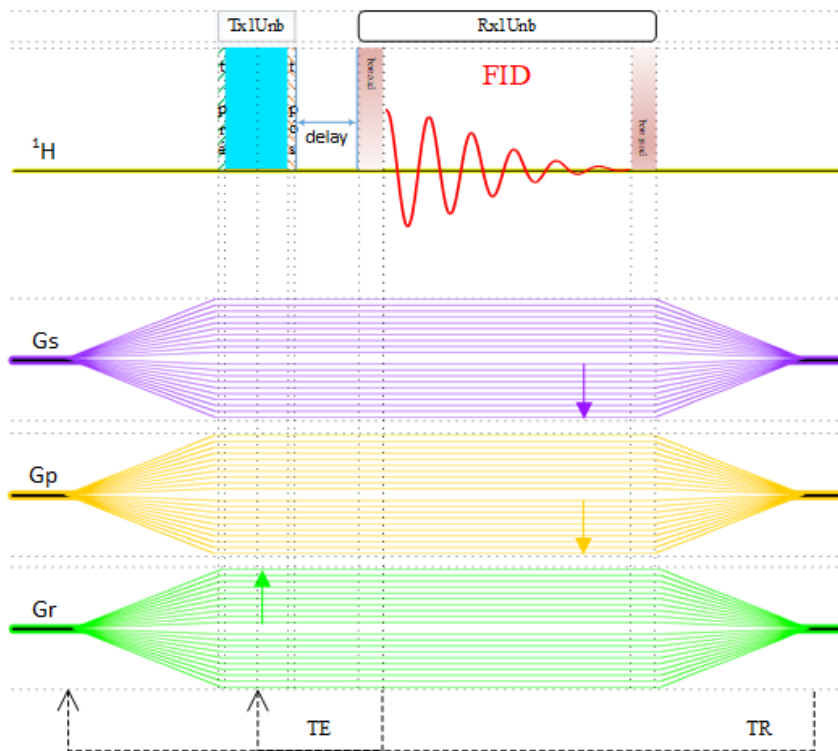


Figure 16 – Pulse program diagram of the Zero Echo Time sequence. The parameter TE reflect the impossibility to switch the transmit-receive with no time consumption, that calls the dead time. In the sequence, all the events occur when the gradients are turned on.

Source: By the author.

Figure 17 shows, for the first time, the Zero Echo Time sequence with the modification proposition. In this case it included the application of the Magnetization Transfer (MT) pulse before the execution of the sequence.⁵⁹ The MT is basically an off-resonance pulse applied to partially saturate the hydrogen pool with very short transverse relaxation time, or with a broad range of resonant frequency.

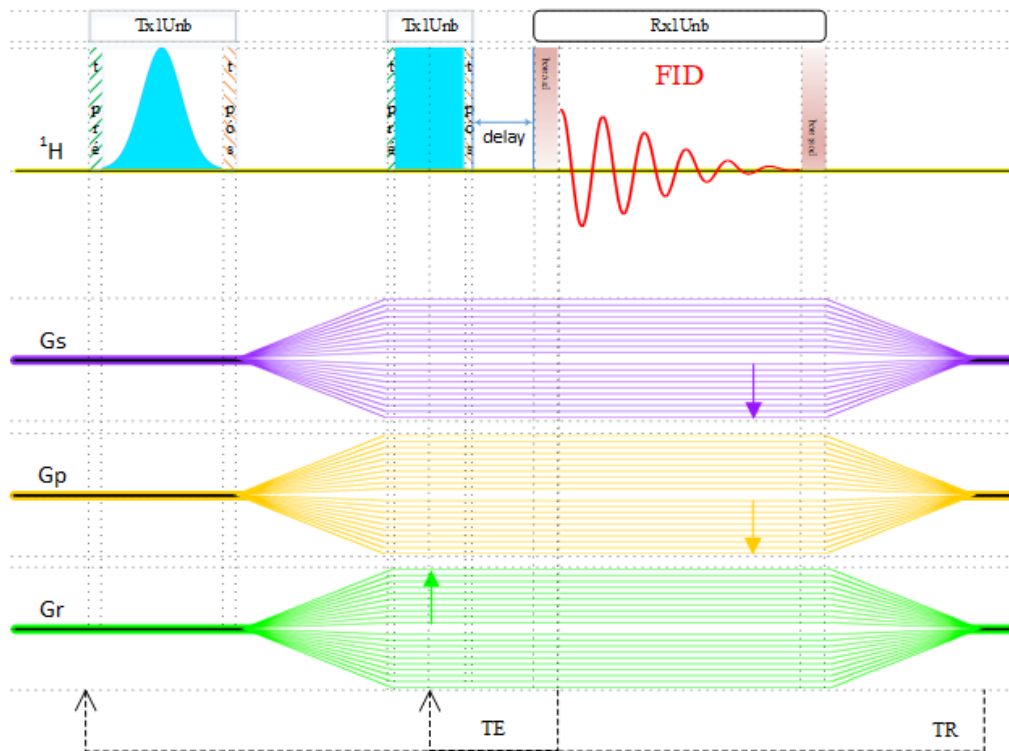


Figure 17 – Pulse program diagram of the modified Zero Echo Time (ZTE) sequence with the application of the Magnetization Transfer (MT) preparation in the form of a Gaussian pulse.

Source: By the author.

The principal sources of the signal in ^1H MR imaging in living tissues and its relative contributions depends of the tissue studied and the particular pulse sequence used. Basically, the signal comes from water that has the major contribution and is found in its free or bound water, lipids, small organic molecules like amino acids, sugars, organic acids, and low-molecular weight proteins and, macromolecules that includes both large proteins as well as extracellular molecules.⁶⁰

Now, consider an object that contain three pools of ^1H nuclei involved in generation of the MR signal that is free water, bound water, and macromolecules. The free water is largely unstructured and the T_2 is very long, with a very narrow range of frequencies near the Larmor frequency. Hydrogen nuclei in macromolecules have a highly restricted motion that results in a shortest T_2 values, representing a broad range of resonant frequencies from Larmor frequency in the order of some kilohertz.

The bound water consists of a water molecule closely associated with the surface of macromolecules. Water in this layer is moderately structured and has restricted motion due of hydrogen bonding with sites on macromolecules. Thus, like

macromolecules, it has short T_2 values and a broad range of resonant frequencies. These waters may undergo both dipole-dipole cross-relaxation as well as chemical exchange with macromolecular hydrogen nuclei.

In a traditional MRI sequence a radiofrequency pulse is applied at the Larmor frequency with energy absorption primarily by free water pool. These excited protons then begin a relaxation process where they release this absorbed energy to the lattice by T_1 relaxation that includes all these three pools. This energy transfer occurs through the microscopic mechanisms like dipole-dipole and chemical exchange interactions. The shifting of energy between pools is known as Magnetization Transfer.

The process described above can be proceed in the opposite direction by applying a specially designed RF pulse, called the Magnetization Transfer Pulse (MTP), to deposit energy first into the macromolecular pool, and the free water will serve as a final step to disperse the injected energy. Depending on the degree of interaction between the pools, the free water pool becomes partially saturated.

Now, following an MTP procedure, if the free water pool is subsequently imaged using traditional sequence, the signal will be reduced due to the saturation, reducing the net magnetization of the free water. The magnitude of this MT effect can be quantified by obtaining two images, with and without the MTP. The magnetization transfer ratio (MTR) is defined as:⁶¹

$$MTR = \frac{S_0 - S_{MT}}{S_0} \quad (47)$$

where S_0 is the magnitude of the signal without the MT pulse and S_{MT} is the signal after the MT pulse. The relative difference of the signal between both images is known as Magnetization Transfer Contrast (MTC). This is not an absolute measurement, and the shape, bandwidth and, frequency could affect the value.

2.3 SEED STRUCTURE AND MORPHOLOGY

A seed could be defined as a mature, fecundated ovule, that contains an embryonic seedling and sometimes a reserve tissues, both protected by a tegument

or pericarp. Basically, the seeds present a unit structure that participates of the dissemination, protection, and the reproduction of species.⁶²

The first step in the formation of a seed is the opening of the flower bud, which means sexual maturity of the mother plant. After fecundation, a series of events occur, such as the formation of the fruit in some cases, the transformation of the zygote into an embryo, the development of the endosperm, and the formation of the protection tissue or shell.⁶³

Generally, the protection tissue of a seed could manifest in two different types of structures, testa and tegmen, that was developed from the ovule tissues, although in many cases it suffers for a considerable reduction in the thickness and a partial structural disorganization, while the embryo and endosperm occupy the biggest fraction of the volume of the seed.⁶⁴

When the ovule has only one integument, the seed may also have only one type of tissue. However, in many cases the ovule components are simplified during the development of the seed, and can be reduced to a thin layer, or disappear entirely, for example, as in corn, where the seed appears firmly adhered to the tiny pericarp of the fruit. Commonly, these tissues turn very dry and hard, protecting the embryo, the vital part of the entirely seed, from solar radiation that could damage the genetical material from thermal variations and also from the action of insects or other external agents.⁶⁵

When the physiological maturity of the seed occurs the funiculus undergoes abscission, leaving a scar called hilum where it separates from the seed, which is generally the region with the greatest permeability of the seed due to the tiny thickness of the integuments, allowing water to enter during imbibition and gas exchange during the germination process.⁶⁶

On the other hand, the endosperm is related to the nutritive tissue of the seed, resulting from the fecundation of the embryonic sac per one male gamete, which takes the formation of a triploid structure, resulting in two types of endosperm know as nuclear and cellular.⁶³

The zygote begins to divide after the beginning of the development of the endosperm, where through mitotic divisions, it results in the formation of the embryo, a process in which it is similar in all plants with seeds. The mature embryo consists of a stem-like axis, with one or two cotyledons, which are the first leaf structures of the plant.⁶²

Early in development, monocotyledon and dicotyledon embryos undergo a similar cell division stage, both of which result in spherical bodies. After that, differentiation occurs, because while the embryo of the dicotyledons develops the two parallel cotyledons, the embryo of the monocotyledons becomes cylindrical, forming a single one. After complete embryo development, future plants can only develop due to the presence of undifferentiated cells in the two poles of the embryo, called shoot apical and root apical meristems.⁶²

In dicotyledonous seeds, such as soybean, the apical meristem can be seen as a residue of the embryonic tissue where, in some cases, the first embryonic leaves develop a structure that takes the name of plumule. The portion between the plumule and the root is called hypocotyl and when the root can be differentiated it is called a radicle (Figure 18).⁶³

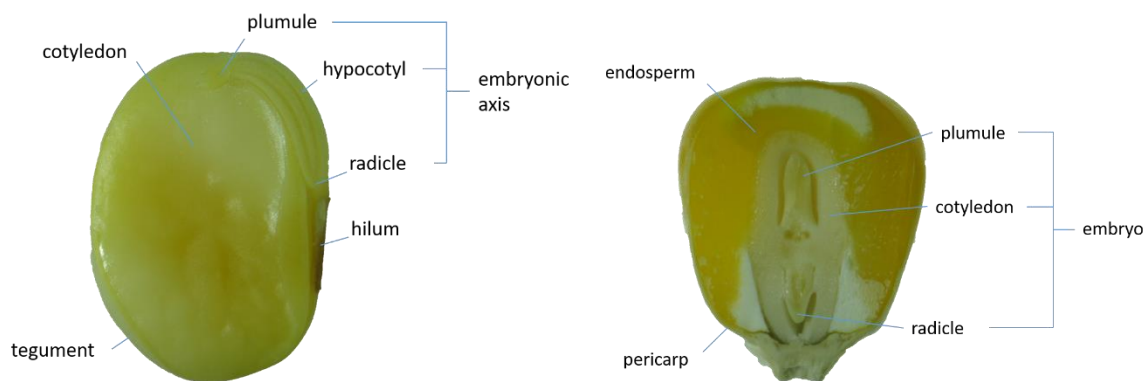


Figure 18 – A cross-sectional view of a soybean (left) and a corn (right) seed. Note the small structures that are constituent elements of the embryonic axis or the embryo in these seeds. This is the most important part of a seed that will result in a new seedling and the propagation of species.

Source: Provided by Francisco Guilhien Gomes Junior.

On the other hand, in monocotyledonous seed, such as corn, the embryo, when fully formed, has a massive cotyledon, the scutellum, attached to the endosperm. In addition, the scutellum connects to the embryo that has a radicle at the bottom and a plumule at the top, surrounded by a protective structure. Corn seed, for example, is associated with the fruit, with the endosperm being the largest portion, formed by an outer layer of aleurone, containing proteins and fats, and a starch layer, together with proteins and carbohydrates.⁶³

Despite the complexity of all these structures that make up seeds, the water, a very simple molecule but of fundamental importance for magnetic resonance due to

the presence of hydrogen atoms, is present in all of these structures in the most varied forms, and the understanding of the water status and the transformations throughout the imbibition process and initial stage of germination may influence subsequent development and growth.

Many studies have been reported, either in low- or high-resolution spectroscopy to comprehend the state of water inside seeds, and the compartmentalization, transport, and mobility of the water inside tissues are described by the standard parameters acquired as transversal or longitudinal relaxation times.⁶⁷⁻⁶⁸

Specific studies on soybean seeds reports the moisture diffusion in dry soybean seed measured by pulsed-field-gradient NMR,⁶⁹ analysis of physical states of water in soybean seeds,⁷⁰ characterization of soybean seeds by nuclear magnetic resonance spectroscopy under accelerated ageing conditions,⁷¹ and changes in seed water status in developing soybean seed grown under moisture stress conditions.⁷²

On the other hand, studies on maize seeds and seedlings reports the relationship between spin-lattice relaxation time and water content,⁷³ ¹H and ³¹P NMR investigation of Gadolinium uptake in maize,⁷⁴ water exchange in plant tissue in the presence of paramagnetic centers,⁷⁵ location of sucrose and oils in maize seed,⁷⁶ and analysis of oil content of maize by NMR.⁷⁷

The most significant findings in these NMR relaxometry studies point to the presence of two or three water proton components in these systems. These NMR studies on seeds show that structural water is associated with the shortest relaxation times, the bound water with the intermedia relaxation times, and free water with the longest relaxation times. Thus, the use of MRI capable of sampling short relaxation times, such as FLASH and ZTE, can contribute to the evaluation of these types of water inside the seeds, as well as lipid distributions.

However, differences in water uptake in high and low vigor soybean seeds in the early stages of hydration, as well as the morphological differences between healthy, immature seeds, and insect attacks need to be further studied to better understanding these differences or the extent of such damage. In addition, a similar analysis is also conducted on corn seeds, due to their significant differences in relation to soybean seeds, with respect to the intrinsic relaxation times of each seed.

3 MATERIALS AND METHODS

The seeds used here were supplied by the Department of Crop Science of the “Luiz de Queiroz” College of Agriculture of the University of São Paulo, Piracicaba, São Paulo State, Brazil. The soybean seeds came from the two lots of a same cultivar, with high and low vigor determined by evaluations of accelerated aging, seedling emergence in the field, electrical conductivity, seedling length, and uniformity of seedling development. The corn seeds were used to support the study of the behavior of the MR signal in the purposed methodology.

In the 2D radiographic analysis, the seeds were evaluated using digital equipment Faxitron X-Ray, model MX 20 DC12 (Faxitron Bioptics, LLC, Tucson, USA), installed at the Image Analysis Laboratory on the Plant Production Department as USP/ESALQ, in Piracicaba, São Paulo, Brazil. To obtain the images, the seeds were positioned 11.4 cm from the source of X-Ray emission after being fixed in the appropriate position on a transparent acetate sheet with 1 mm thickness, using double-sided tape.

The magnetic resonance images were acquired with a 2T field horizontal superconductor magnet from Oxford Instruments, model 85310HR, which operates with a Bruker Avance AVIII (Bruker-BioSpin, Inc., Billerica, MA) spectrometer, a system broadband (2 up to 400 MHz) with two transmission channels (1H and X), four receiver channels (1H or X, any combination), four-channel parallel acquisition, 300 V / 200 A gradients amplifiers, 12 shimming channels, 16 Gauss / cm gradients, two 1 and 2 kW radiofrecuencie amplifiers. The software used for image manipulation and reconstruction was Paravision 5.1.

In order to adapt the dimension of the seed sample, enhance the fill-factor and improve the signal-to-noise ratio (SNR) a small solenoid coil was developed. It consists of a 5 turns AWG 36 of cooper wire with 10 mm of diameter per 10 mm of length and two variable capacitors for the adjustment of the matching and tuning of the coil (Figure 19).

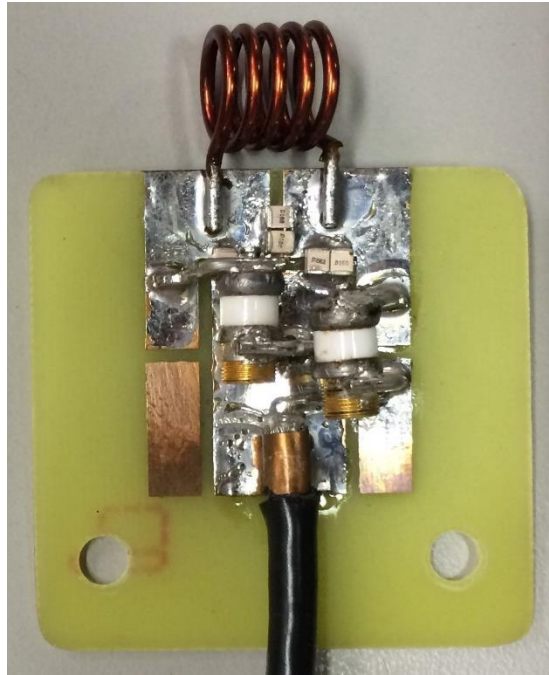


Figure 19 – The solenoid coil used to acquire the Magnetic Resonance Images. Two variable capacitors were placed to manually adjusted the tuning and matching when the coil and sample are placed into the magnetic field.

Source: By the author.

The tuning and matching are determined by measuring the reflection parameter S_{11} . The results obtained are direct measurements observed with the *Network Analyzer* from the company *Agilent Technologies*, model E5061A, adjusted at the frequency of 85.2 MHz with a span of 20 MHz.

The FLASH sequence was optimized with the follow parameters: TR = 75 ms, TE = 3 ms, flip angle = 45° , 8 averages, and 2 hours and 43 minutes of acquisition time. The field of view (FOV) used was $12.8 \times 12.8 \times 12.8 \text{ mm}^3$ with a matrix of $128 \times 128 \times 128$ points, resulting in an isotropic spatial resolution of $100 \times 100 \times 100 \text{ }\mu\text{m}^3$. The radiofrequency pulse used here was a Hermite pulse with 200 μs length duration. Here, the images were zero-filled in all directions of the data matrix as the same length of the acquired data before the application of the Fourier transformation.

Even with the optimization of the parameters of the FLASH sequence, it was still necessary to hydrate the soybean seed to obtain good quality images. Then, each seed was placed in a plastic box with a lid and, a piece of paper towel that was moistened with a water mass of 2.5 times its weight. The hydration period was 3 hours, resulting in a water content in the seeds of approximately 18 %.

The ZTE sequence was optimized with the follow parameters: TR = 20 ms, TE (dead time) = 640 μ s, the flip angle was manually adjusted to produce the maximum signal in the acquisition, 16 averages, and 3 hours and 28 minutes of acquisition time. The FOV used was 25.6 x 25.6 x 25.6 mm³ with a matrix of 256 x 256 x 256 points, producing an isotropic spatial resolution of 100 x 100 x 100 μ m³. The radiofrequency pulse used here was a Hard Pulse with 2 μ s of length duration. When using the Magnetization Transfer Contrast (MTC) preparation before the ZTE, the pulse used was a single gaussian pulse with RF peak amplitude of 500 μ T, irradiation offset of 3000 Hz, 10 ms of length duration, resulting in a selective bandwidth of 274 Hz.

The relaxometry experiments were conducted with a minispec magnet from Bruker, which operates with a LapNMR spectrometer from TECMAG in a frequency of 19.9 MHz. The methodology used here was developed by Montrazi, E. T., et al⁷⁸ (Figure 20), in order to acquired simultaneous T_2 - T_2 exchange or T_1 - T_2 correlation by taking the advantage of the storage time and the two steps phase cycling used for running the relaxation exchange.

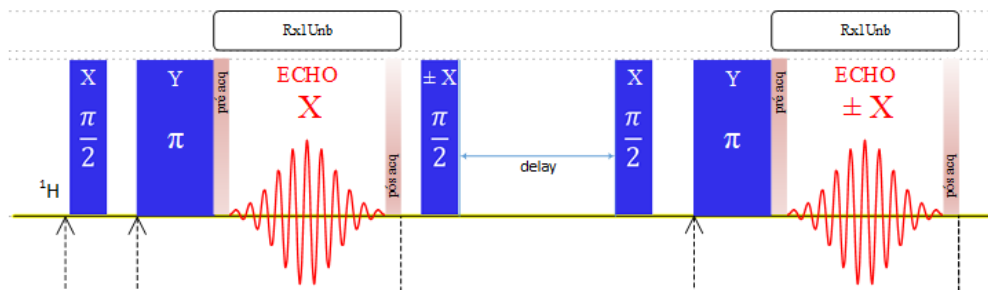


Figure 20 – Time diagram of the Transverse Relaxation Exchange (TREx) sequence. Basically, it consists of the application of two Carr-Purcell-Meiboom-Gill (CPMG) with a phase modulation in the second excitation pulse and echo acquisition. The summed or subtraction of the two data set results in T_2 - T_2 exchange or T_1 - T_2 correlation.

Source: By the author.

Thus, ten soybean seeds from each group were selected to carry out the relaxometry experiment. Due to the duration of the analysis, which was about 10 minutes, measurements were made in two days for each group, resulting in a total of 4 days for the analysis of the two groups.

The seeds were placed in a plastic box with three sheets of paper towel, two being the bottom and the last as a cover. The sheets of paper were moistened with a

water mass of 2.5 times their weight. Thus, at each analysis, the box was opened and a seed was removed for the resonance measurement. The process was repeated 6 times, resulting in 7 hydration curves, where it was also considered the measure of the seed in the storage condition, or before the hydration process.

4 RESULTS AND DISCUSSION

The result and discussion chapter will be divided into three parts, the first section talks about the coil characterization, some parameters that is useful to understand how an MRI instrument needs to be set up. The second section talks about the evolution of the optimization of sequence parameters, and the results acquired with the images in a deeper fashion. The last one section talks about the results acquired with the relaxometry to understand differences between seeds with high and low vigor.

4.1 COIL CHARACTERIZATION

The characterization and tuning for the frequency operation of a new coil is essential both to avoid power losses due to reflection during the transmission of the radiofrequency pulses and also to maximize the signal-to-noise (SNR) ratio during the reception of the Nuclear Magnetic Resonance signal.

The tuning and matching are determined measuring the parameter of the reflection S_{11} . The obtained results are showing in the Figure 21 in the Smith Chart, that provides the complex impedance of an electrical instrument, and in a logarithmic scale, that give the information about the return loss when the coil is tuned on the frequency operation.

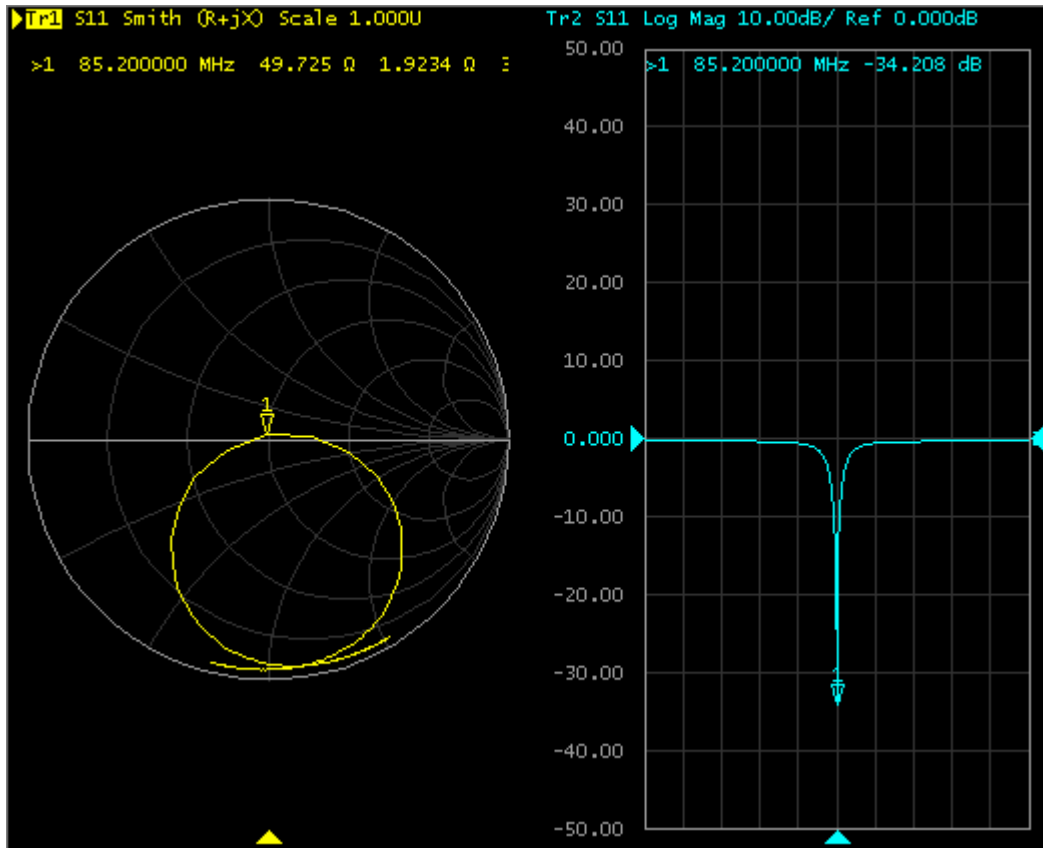


Figure 21 – Image of the Smith Chart (yellow line) that provides the complex impedance and logarithmic scale (blue line) of the measurement of the reflection parameter S_{11} at the frequency of 85.2 MHz captured by the Network Analyzer.

Source: By the author.

The most important results obtained here with the coil characterization are summarized in Table 2.

Table 2 – Reflection coefficient and values of real and imaginary part of a complex impedance acquired with a direct measurement of the solenoid coil when tuned with the frequency operation.

	S_{11} (dB)	Re {Z} (Ω)	Im {Z} (Ω)
Solenoid Coil	-34.2	49.7	1.9

Source: By the author.

Another parameter that is useful to know is the quality factor, which allows to evaluate the losses of the coil when used, for example, the interaction with the main magnetic field that can create induced currents and is related to the dissipation of transmitted power, or with the materials that were used to build the coil. In addition, the measurement of the frequency displacement was performed due to the fact that

this value is associated with the coupling of the coil with the sample. The results are shown in Table 3.

Table 3 – Quality factor of the coil with unloaded and loaded condition, and frequency displacement.

	Q_{unloaded}	Q_{loaded}	Δf (KHz)
Solenoid Coil	156	144	70

Source: By the author.

Finally, the measure of the signal-to-noise ratio was performed with the sequence *Multi-Slice Multi Echo* (MSME) using the following parameter: TR = 1000 ms; TE = 14 ms; TA = 4 minutes; Field-of-View (FOV) = 3 x 3 cm²; data matrix: 256 x 256; and spatial resolution of 117 x 117 μm^2 (see Figure 22). The image was carried out with a small phantom filled with a solution of water with copper sulfate at a concentration of 1 g/l.

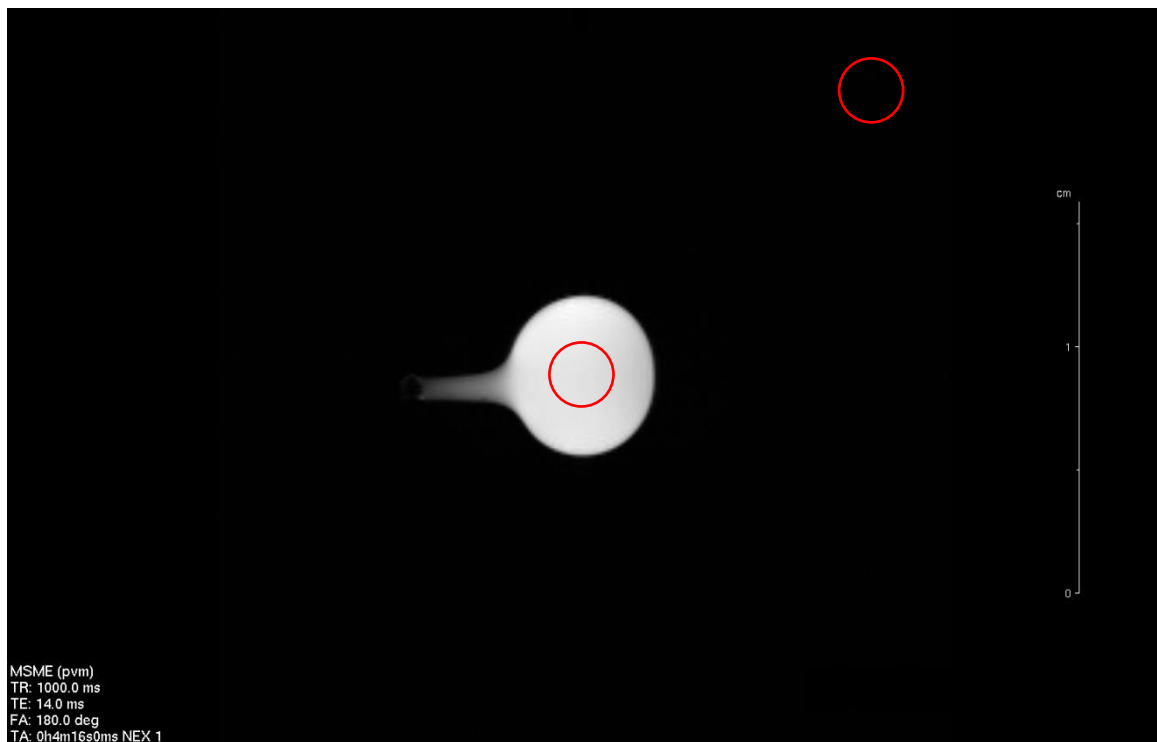


Figure 22 – Image of the spherical phantom with 7 mm of diameter filled with a solution of water with copper sulfate at a concentration of 1 g/l.

Source: By the author.

Two regions of interest (ROI) were used, one in the center of the phantom to avoid partial volume next to the edge of the object, and order close to the edge of the image. The value was computed using the Equation 47:

$$SNR = \frac{\bar{S} - \bar{N}}{\sigma_N} \quad (48)$$

In this expression, \bar{S} represent the average signal in the region of the sample, \bar{N} represent the average signal in the region outside the sample, and σ_N in the standard deviation in the same region of average noise. Also, the measure of how much potency was used for the excitation and inversion pulses were performed, and the results are shown in Table 4.

Table 4 – Signal-to-Noise (SNR) ratio and potency used to the application of the excitation and inversion pulses with the sequence MSME.

	SNR	90° (dB) / W	180° (dB) / W
Solenoid Coil	428	74.7 / 1.02x10 ⁻⁵	64.7 / 1.02x10 ⁻⁴

Source: By the author.

The results present above reflecting an excellent SNR and fill-factor which can return better images of MRI, that is a result of a very small signal originated in the object by the application of an RF perturbation in the presence of an externa magnetic field.

4.2 IMAGES RESULTS

Before starting to present the images of real situations of soybean and corn seed, it will be discussed about the types of tissues, reserve material, and most importantly the intrinsic relaxation times that make up these structures in the seed and the behavior of each type of optimized sequence used.

In the first case, the Figure 23 shows two images of different corn seeds acquired with the FLASH sequence (23-A) and with the ZTE sequence (23-B). In the case of the FLASH method, the seed was hydrated for 4 hours before the image acquisition, which results in a water content in the seed of about 18 %. In the case of

the ZTE method, an image was acquired without the need for hydration, with the seed having a water content about 9 %, which is similar to the storage conditions.

Therefore, even with the prior hydration of the seed, the image with the FLASH sequence is not able to sample the signal from the region of the seed endosperm, since there the relaxation times are quite short, and the sequence needs 3 milliseconds to start signal acquisition (echo time), long enough for that signal to disappear before sampling. However, in contrast, the region of the embryo can be observed due to the significant presence of lipids, which also produce magnetic resonance signal, due to the presence of hydrogen in its composition.

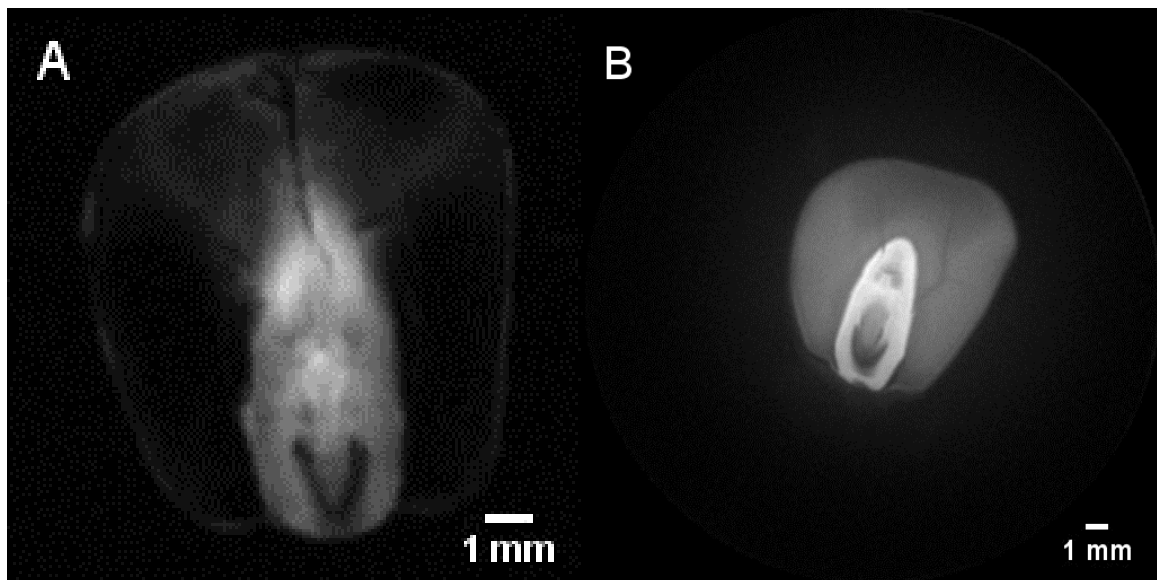


Figure 23 – A corn seed image acquired with the FLASH sequence (left) and with the ZTE sequence (right).

Source: By the author.

Using the ZTE sequence, it is possible to achieve a new perspective in relation to the image of the corn seed, since due to its very short time between signal preparation and acquisition, in the order of 500 microseconds, the region of the endosperm can be observed (brighter region of the seed in Figure 23-B). Furthermore, this preparation time is sufficient for the appearance of contrast between the regions of the endosperm and embryo.

In the second case, Figure 24 shows two images also of different soybean seeds acquired with the ZTE sequence (24-A) and with the FLASH sequence (24-B), but here the results achieved were completely different. With the use of the ZTE sequence, since the time between preparation and readout of the signal is quite

short, little differentiation occurs due to the phenomenon of relaxation, and the resulting image does not present contrast between the different tissues inside the seed, as it can be notice by the practically constant brightness throughout the image (Figure 24-A).

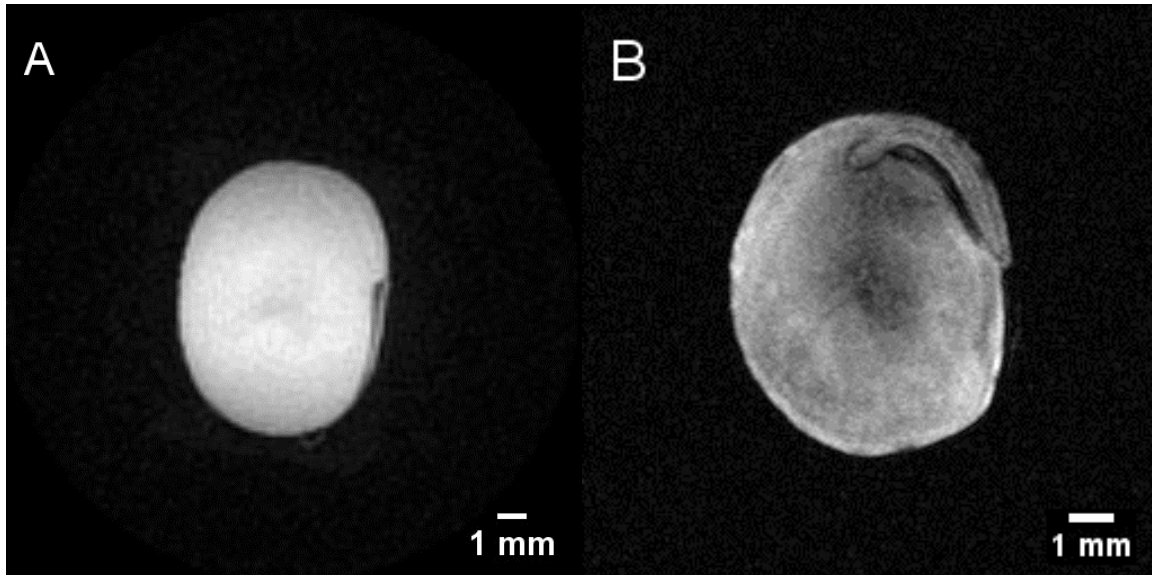


Figure 24 – A soybean seed image acquired with the ZTE sequence (left) and with the FLASH sequence (right).

Source: By the author.

With the use of the FLASH sequence, it is possible to observe differences in brightness in all regions of the seed (Figure 24-B), which means that there are regions with more or less protons, as a result of different densities. Marcos-Filho⁷⁹ describes that the hydration process occurs gradually, with the initial moistening of the tissues closest to the surface and the establishment of a hydration gradient as the water moves into the seed.

So, due to these preliminary results for both optimized sequences, which considered the intrinsic differences of the seeds and their results in the images, the choice was made to make images with the soybean seeds with the FLASH sequence, hydrating the seed for a period of 3 hours before image acquisition and, for corn seed, the sequence ZTE was used because it was not necessary to hydrate the seed.

The results below show a set of images of soybean seeds of the same lot but at different conditions. In the case of the MRI images, each orientation was acquired by transposition of the data matrix before the reconstruction of the image. All images

were zero-filling in all directions as the same length of the acquired data points before the application of the Fourier transformation.

The Figure 25 shows a standard X-Ray image (Figure 25-A) compared with the MRI image (Figure 25-B, C, and D). Despite the high resolution of the X-Ray image, the result is very dependent of the position of the seed before the image acquisition. Also, the image is limited to the observation plane and it implies in the difficult to identify the internal structures or the structure of the embryonic axis. Moreover, due to the little changes in the density of the tissue, the aspects of the image seem to be the same on the entire seed.

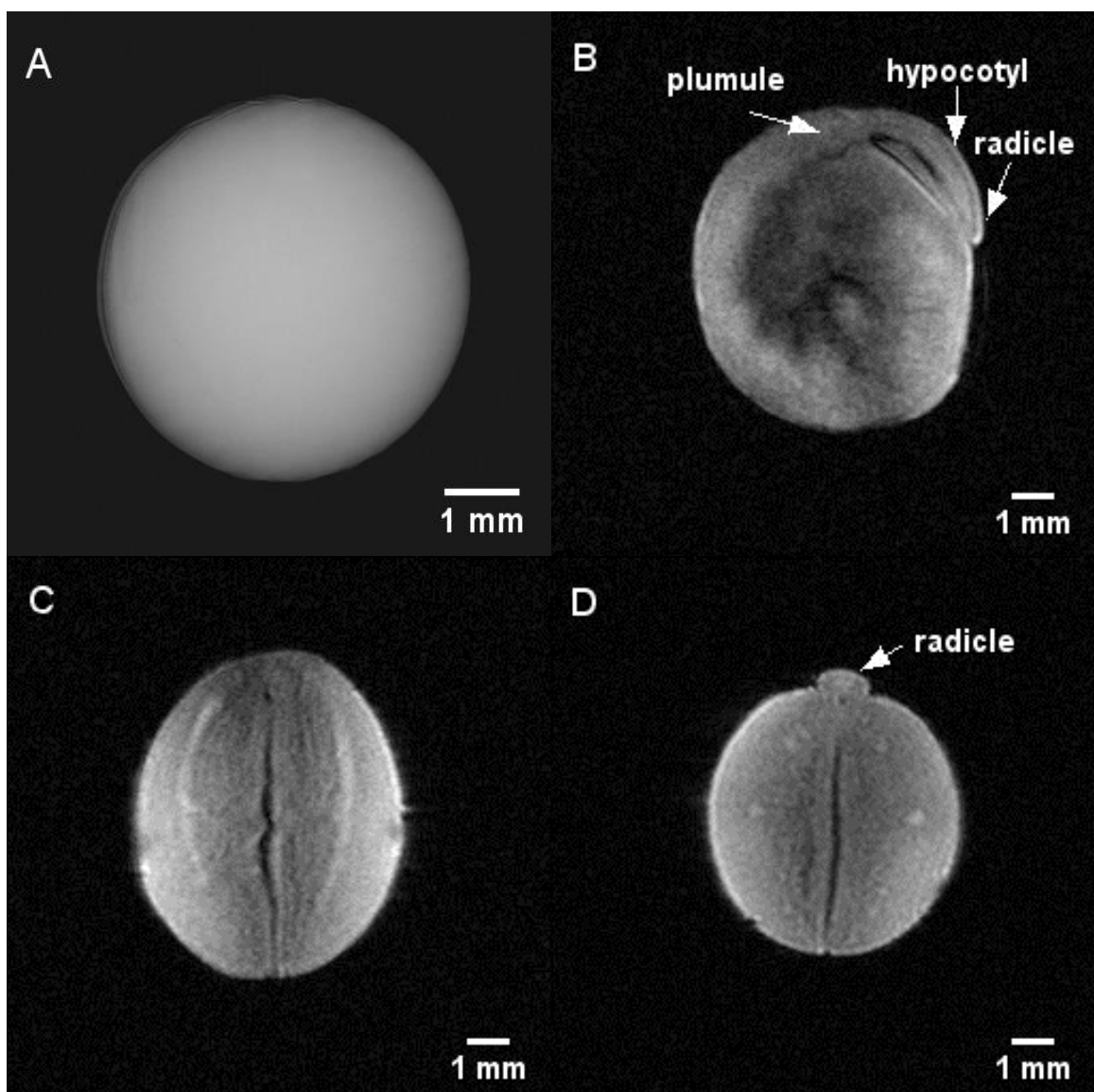


Figure 25 – A standard X-Ray image (A) of a healthy soybean seed compared to MRI image (B, C and, D). The MRI image was acquired with 8 averages, resulting in a 3 hours and 28 minutes of acquisition time.

Source: By the author.

On the other hand, with the MRI image is possible to observe the seed in the three spatial directions, like the directions sagittal, coronal, and axial in humans' exams. Moreover, due the fact that this image is proton density weighted, is possible to observe the internal distribution of the hydrogen atoms and the small differences across the seed tissue.

Also, in Figure 25-B is possible to observe almost the entire structure of the embryonic axis, mainly the radicle and hypocotyl, except the case of the plumule because in the MRI image the reduction of signal is related to the plumule cavity. The brightness in the external parts of the seed is related to the water that was absorbed during the imbibition time before the image acquisition.

The Figure 26 shows a standard X-Ray image (26-A) and an MRI image (26-B, C and, D) of a soybean seed with a severe damage due a chinch bug bites. In both images is possible to visualize the regions on the seed structures that tissues were compromised by the damage. But, exists a limitation on the X-Ray image in assess the depth and the internal structures that were affected by the damage, resulting in an incomplete evaluation of the injury.

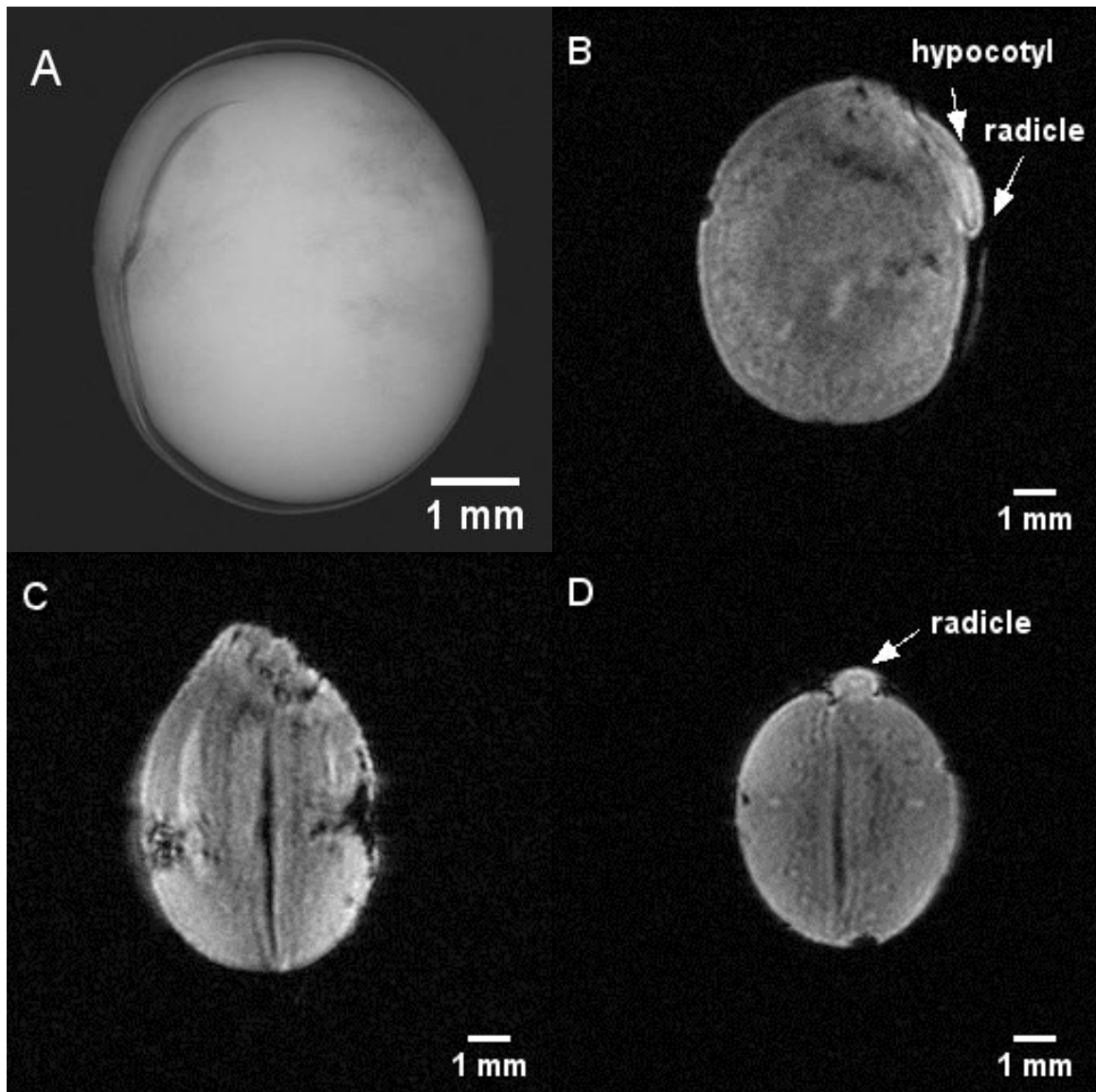


Figure 26 – A standard X-Ray image (A) of a soybean seed damaged by chinch bug bites compared to MRI image (B, C and, D). The MRI image was acquired with 8 averages, resulting in a 3 hours and 28 minutes of acquisition time.

Source: By the author.

With the images by MR is possible to observe the entire extension of the injury in both cotyledons, and also the depth of the injury, by the destruction of the internal tissues and of the entrance of air, and if the damage occurred in the regions next to the embryonic axis, that could result in the dead of the seed.

Another problem that can be identified, related to structural damage to the internal tissues in the seeds, is the presence of mechanical damage without the loss of material, which has already been shown in previous results.⁸⁰

Although the immature soybean seed could be identified without any elaborated technique due the fact, for example the green color of the cotyledon

tissues, the MRI technique can explore further if the internal conditions of the seed or the vital structures that were developed in the process of seed formation (see Figure 27).

Several factors can contribute to the occurrence of greenish soybean seeds, among them the combination of drought associated with high temperatures in the final stage of seed maturation, which results in the premature death of plants and forced maturation, or by the deactivation of enzymes responsible by the degradation of chlorophyll. Some diseases can also result in this problem, such as fungi, root rot, or even leaf diseases. The severe attack by insects, main by chinch bugs, also leads to this problem.⁸¹

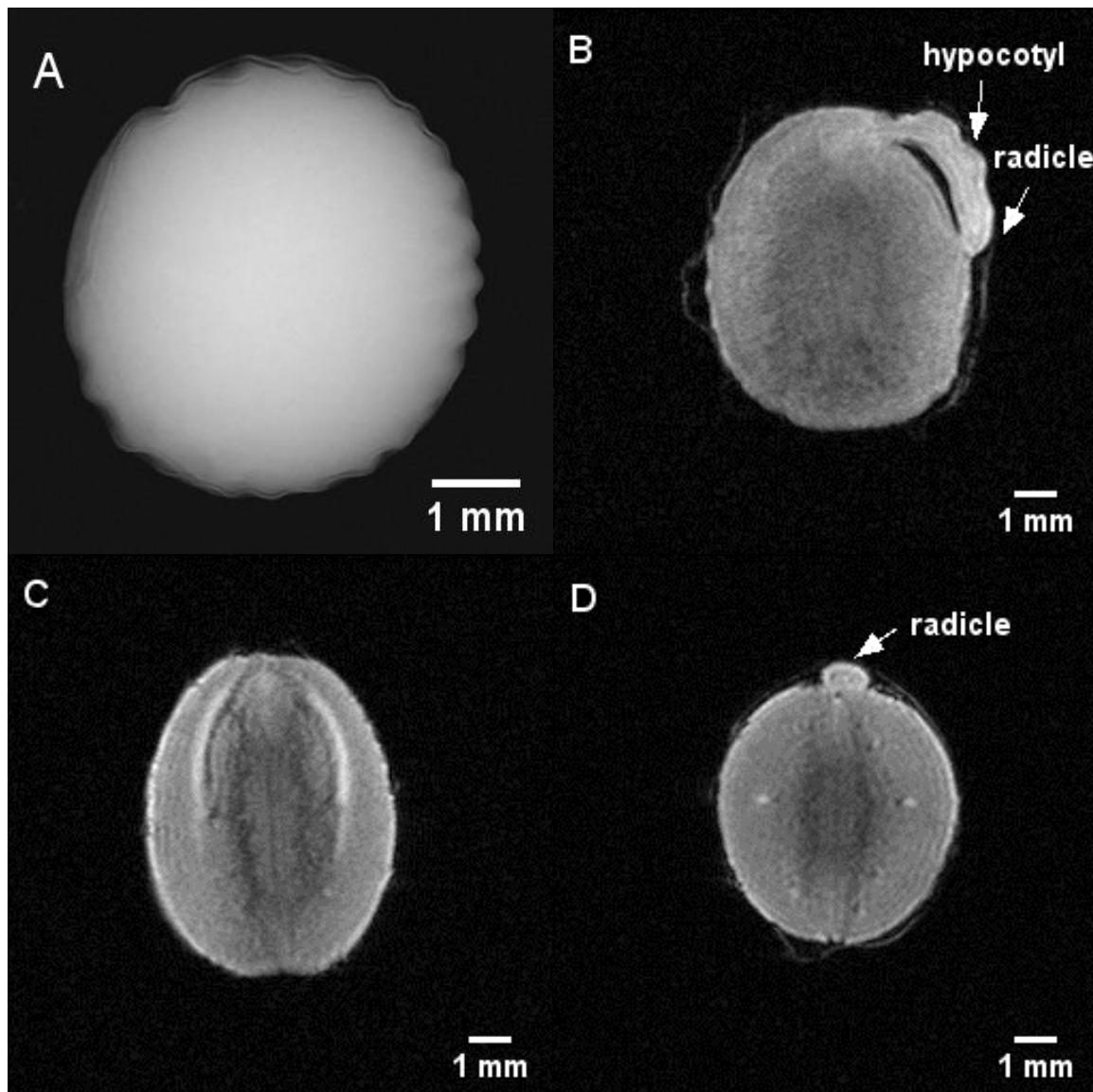


Figure 27 – A standard X-Ray image (A) of an immature soybean seed compared to MRI image (B, C and D). The MRI image was acquired with 8 averages, resulting in a 3 hours and 28 minutes of acquisition time.

Source: By the author.

Compared to the X-Ray image (Figure 27-A), the MRI images (Figure 27-B, C, and D) shows clearly that the internal structures of the cotyledon are the same as a seed with healthy aspects, although it is possible to observe a less development of the embryo region compared to the healthy seed on Figure 25 as a result of malformation. But other tissues inside the cotyledon region were well developed.

In the MRI, the seed has no wrinkling of the seed coat, due to the fact that the seed was previously hydrated to acquire the image, but it is still possible to notice some wrinkling in the hypocotyl of the embryonic axis (Figure 27-B), which may be related to a malformation of this structure, which can cause a slower germination and low vigor when compared to a healthy seed.

The Figure 28 shows the X-Ray image (A) of a healthy corn seed, that has a good resolution but the internal structures suffers from the absence of contrast, for example, it is possible to observe the region of the plumule but the region of the radicle is not clearly resolved. Also, due the fact of low-density differentiation of the region of the endosperm, this portion of the image appears as the same brightness of the cotyledon without any contrast.

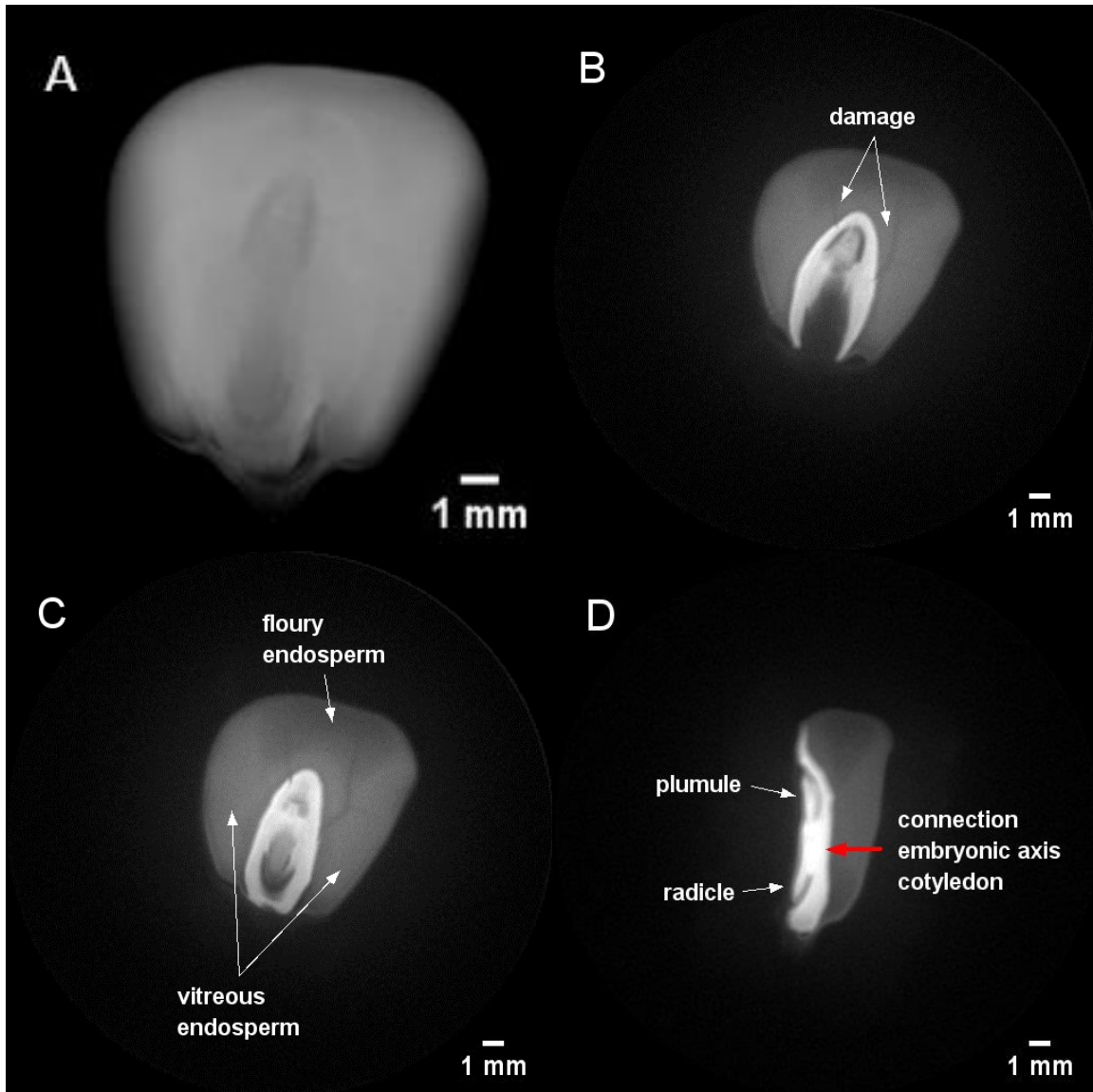


Figure 28 – A standard X-Ray image (A) and the MRI image (B, C and, D) of healthy corn seed. It is possible to observe a damage in the region of the endosperm above the plumule that is not observable with the X-Ray image.

Source: By the author.

On the other hand, the MRI image (Figure 28-B, C, and D) show much more details of the internal structure of the corn seed. First, it is possible to clearly observe with a good resolution and contrast the entire structure of the embryo. In the region of the endosperm, two interesting details are shown in the image (Figure 28-B, and C), that is the internal damage and the differentiation of the floury and vitreous endosperm, that is not appear in the X-Ray image.

Also, turning the direction of the image it is possible to observe the connection of the embryonic axis with the cotyledon of the seed (Figure 28-D), and the structures of the plumule and radicle appear like a little floating finger. Furthermore, the MRI

image show a very different contrast between the region around the embryo (embryonic axis plus cotyledon) and the endosperm, proof that the region of the embryo has the largest relaxation times than the region of the endosperm.

For evaluated an example of internal damage to corn seed, Figure 29 shows a seed that presents one of the worst problems in the storage or international transport of seeds and grains, which is the presence of the weevil larvae deposited by the female insect.

The entire inoculation process was prepared by ESALQ-USP collaborators. After the procedure, the seed was stored under favorable conditions for the development of the larva until the initial stage, where the insect begins the process of deterioration and consumption of the internal material of the seed reserve.

With the X-Ray image (Figure 29-A), despite its simplicity is possible to visualize that the seed has a problem, but it is very difficult to identify precisely regions inner the seed that was compromised by the presence of the weevil larva in development. In addition, the regions where damage can be seen are those that have been severely affected, compared to regions close to the embryo that appear to have suffered less (Figure 29-B, C, and D). Moreover, in the X-ray image it is not possible to observe any damage in the region of the embryo, which could lead to the conclusion that this seed could still be germinated.

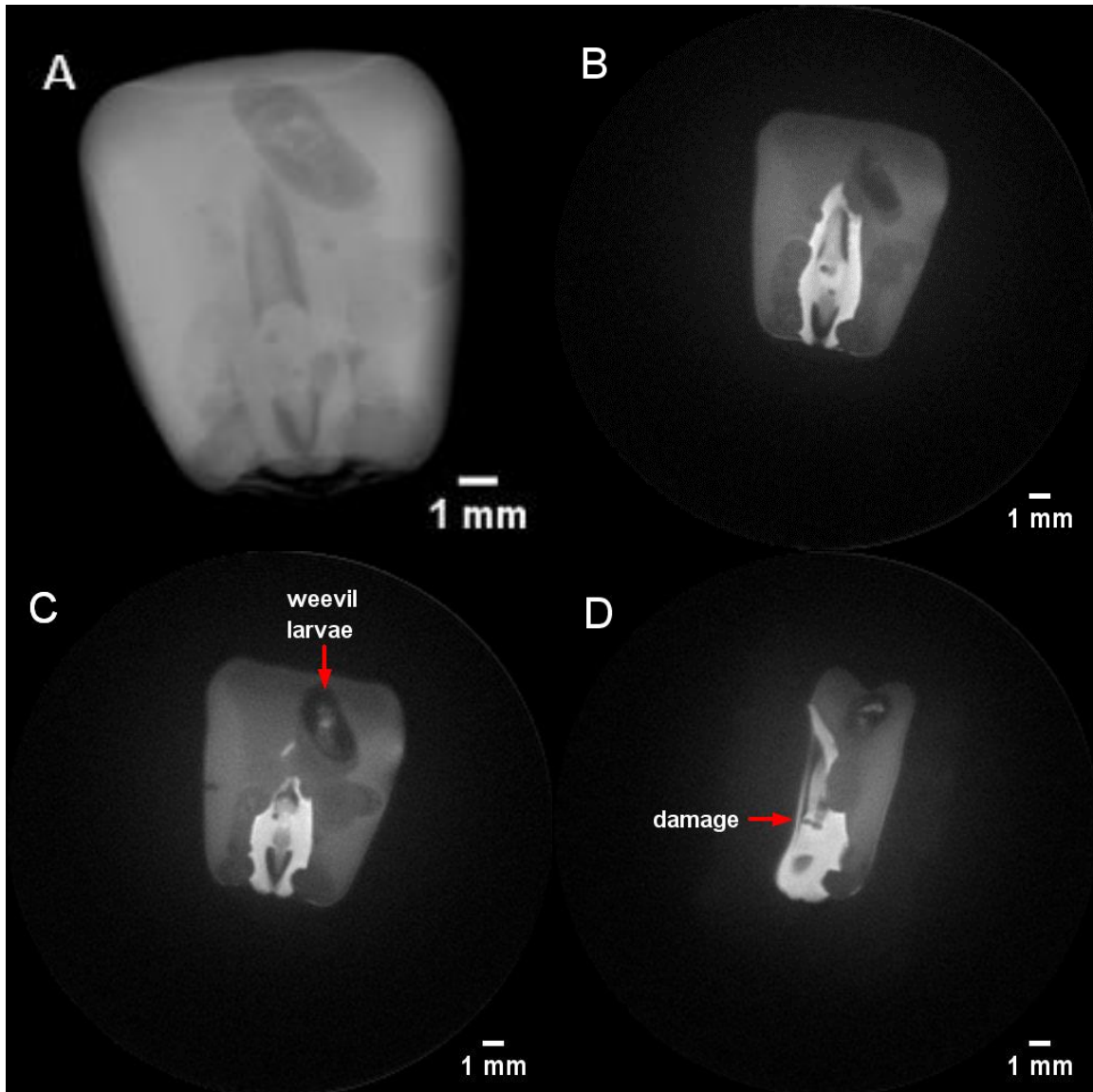


Figure 29 – A standard X-Ray image (A) and MRI image (B, C and, D) of corn seed with a weevil growing inside, destroying much of the internal tissues before hatching in its adult form.

Source: By the author.

The MRI brings a new perspective, showing the hard and soft damage that occurs internally in all the different regions of the seed by variation of the intensity of the signal. It is possible to make a more accurate assessment of the involvement of the regions of the endosperm and also of the structure around the embryo, where it is possible to observe a damage at the base of the plumule caused by the larvae, as can be seen in the last image (Figure 29-D), which will certainly result in the seed being unfeasible.

Now, the two sets of images below show (Figures 30 and 31), for the first time, the combination of the ZTE sequence together with the preparation module known as

Magnetization Transfer (MT) or Macromolecular Saturation. The MT was useful, for instance, to analyze fresh and aging wheat, due to changes in the interaction of the water and macromolecules like gluten and flour.⁸²

In Figure 30, the left side (A and C) are the images of the corn seed with the ZTE sequence without the application of the MT pulse. The seed is the same as shown in Figure 28, and all the description was made early. But, here the major advantage, due to the characteristic of the ZTE sequence, all the tissues of the seed contribute to the MR signal at its maximum amplitude.

The images in the right side (B and D) are those that was created with the ZTE sequence with the application of the MT preparation pulse. Note the saturation effect in the region of the endosperm with a reduction of the MR signal coming that area, showing that this region has a very low relaxation times compared to the region of the embryo.

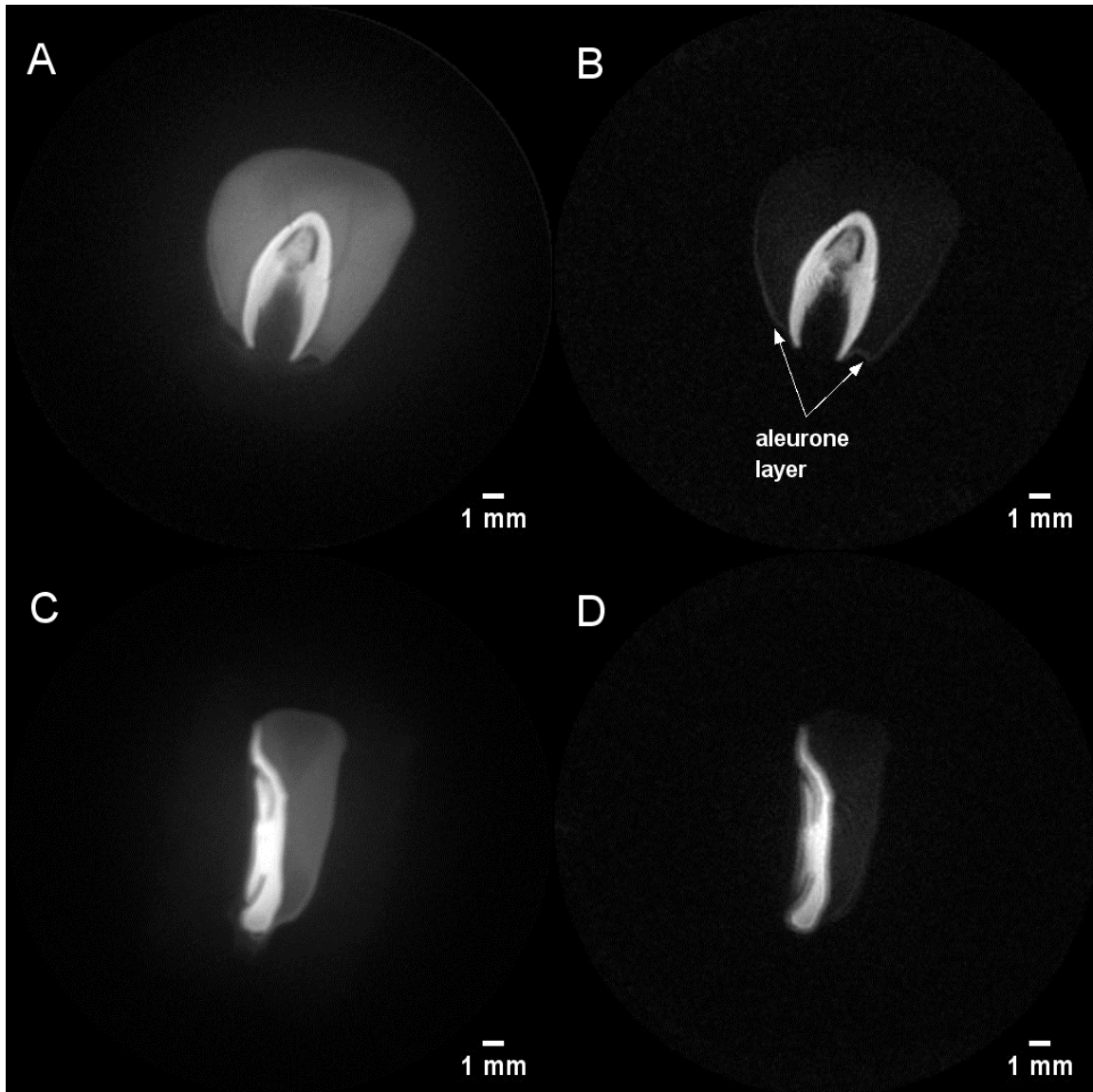


Figure 30 – A corn seed without (left) and with (right) the application of the Magnetization Transfer (MT). Note the reduction of the signal that comes from the region of the starch due the saturation by the off-resonant pulse, and the presence of the signal that comes from the aleurone layer of the seed.

Source: By the author.

The incomplete saturation of the region described above can be justified by the fact that in the applied sequence, only a single pulse was used for MT, so the replacement of a single pulse by a train of pulses could result in greater saturation of that region. In addition, it is possible to observe the aleurone layer in the corn seed with the application of the MT pulse (Figure 30-B), since this layer consists of proteins, a greater amount of water may be associated with it compared to the glassy region of the endosperm which is rich in starch.

The aspect of the signal-to-noise ratio may be worse due to the fact that now a smaller amplitude of the nuclear magnetic resonance signal, due to the saturation caused by the MT pulse, contributes to the formation of the image, since the region of the endosperm consists of a considerable fraction of the corn seed, result in an increased level of the noise in the image.

The Figure 31 shows the same idea that the set of images for corn seed (Figure 30), but now with the soybean seed, the left side (A and C) is the image without the application of the MT pulse in combination with the ZTE sequence, and the right side (B and D) of the figure represents the same slice, but now with the application of the MT pulse before the application of the ZTE sequence.

Note the absence of contrast in the images without the application of the MT-ZTE (Figure 31 A and C), despite the fact that this image has a high signal-to-noise ratio, it is basically hidden either all the internal details in the region of the cotyledons or the details of the structure of the embryonic axis.

On the other hand, the images on the right side (Figure 31 B and D) shows again the details inside the region of the cotyledons, when the suppose is to exists a differentiated tissue specialized in the transport of the reserve material to the embryonic axis, like the vessels in the human body. Also, these images were acquired without any hydration, as the images of the soybean acquired with the FLASH sequence.

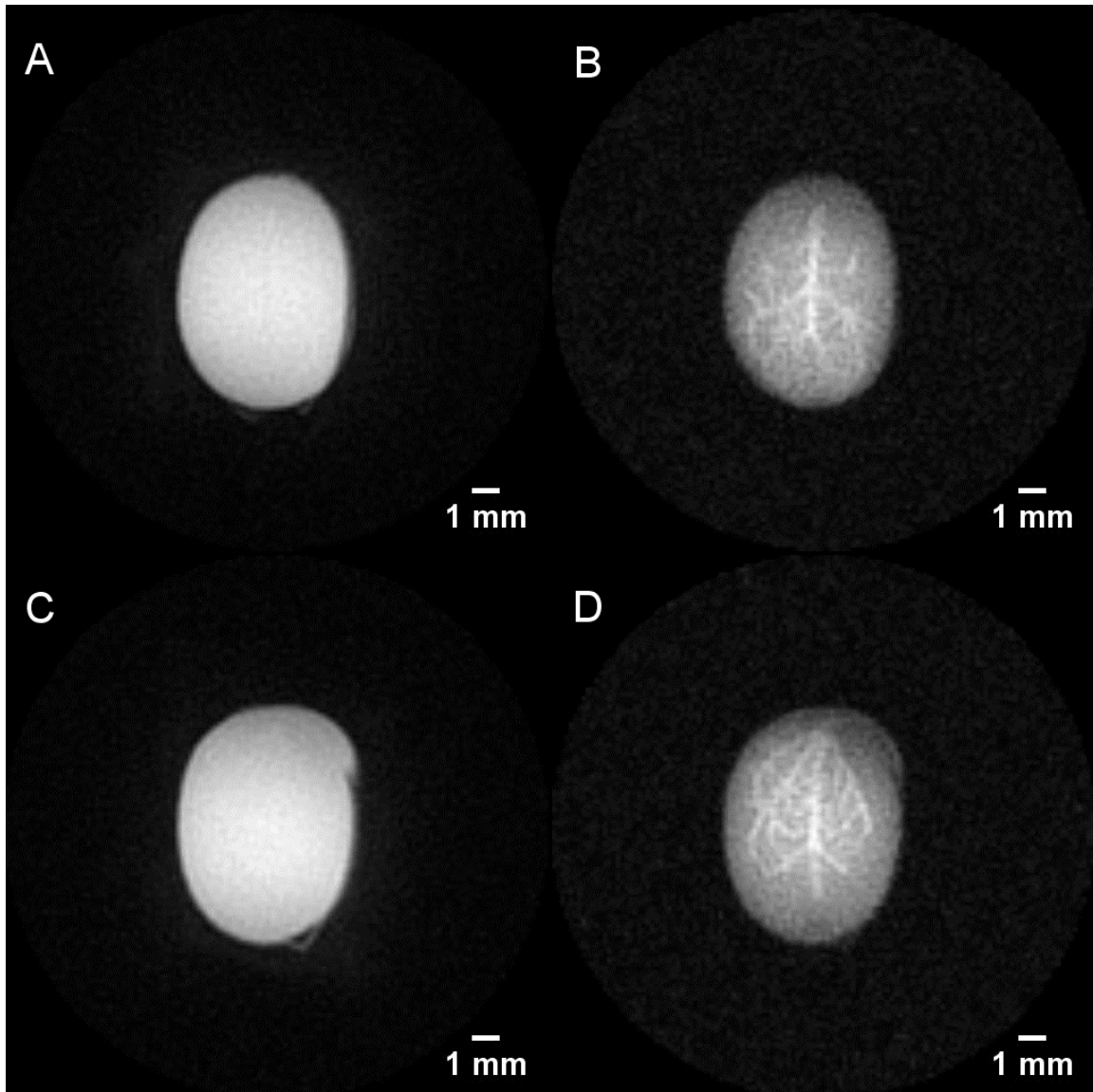


Figure 31 – The same slice of a soybean seed without (left) and with (right) the application of the Magnetization Transfer (MT) before run the ZTE sequence without hydration. The image has only two averages with acquisition time of 34 minutes and 35 seconds.

Source: By the author.

Other aspect that could be pointed out is the result contrast, but the image above was acquired with just two averages, resulting in 34 minutes of acquisition time, reflecting in an approximately 79 % of the reduction time compared to the same contrast reached by the FLASH sequence, but with no necessity of hydration. Thus, the contrast of the image could be improved by increasing the number of averages, but sacrificing the acquisition time.

However, the most important fact here is the observation of the internal differentiated structures in the cotyledon region without any addition of water, as the understanding was that these regions only manifested when the seed was in contact

with the water, and the process of transportation of reserve nutrients and germination started. With these images it is possible to establish that these structures exist in any condition of the seed, in order to maintain the vital process of the seed even in the dormant condition.

4.3 RELAXOMETRY RESULTS

The top graph on Figure 32 shows the evolution of the transverse relaxation time T_2 during the 6 hours of hydration of a seed from high vigor lot. From the image it is clear that the peak on the left is related to the water due the fact that it increases in amplitude and shift for the longest values of relaxation times, while the peak on the right remains unchanged during this period and is related to the oil content of the seed.

The bottom image on Figure 32 shows the evolution of the longitudinal relaxation time T_1 during the time of imbibition of the seed. Despite the fact that in seeds exists a contribution of water and oil on the magnetic resonance signal, both quantities relax with approximately the same longitudinal relaxation times, independent of the concentration of water on the seed tissue.

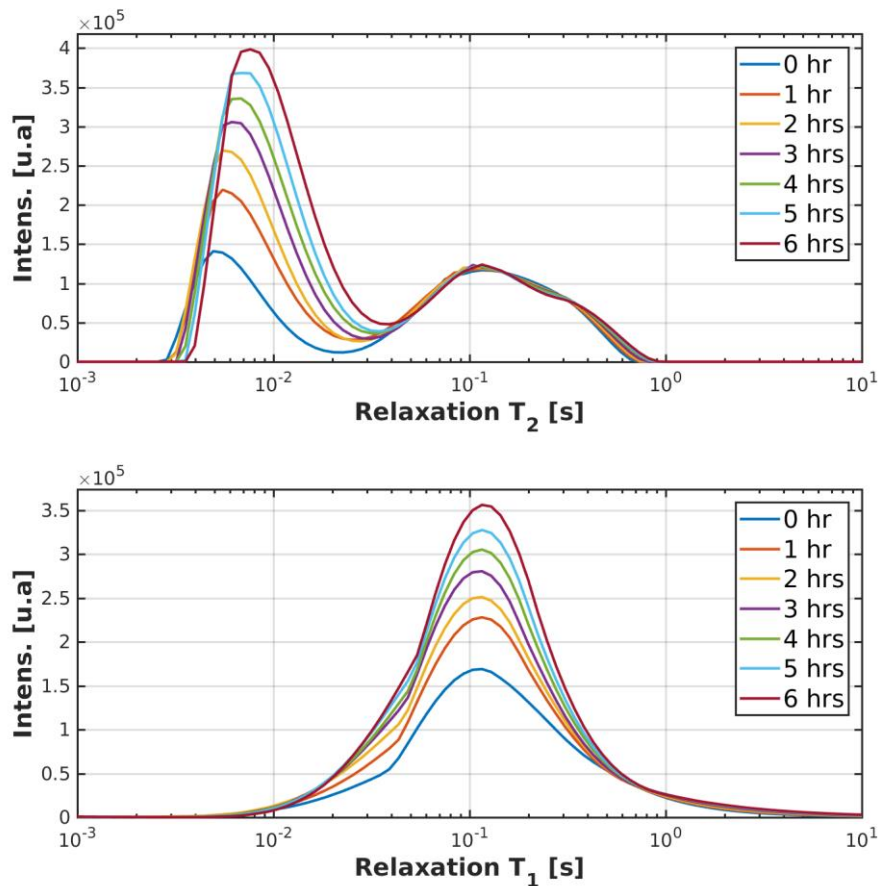


Figure 32 – Relaxation time curves for both T₂ and T₁ obtained by Inverse Laplace Transformation (ILT) for a single seed with high vigor during 6 hours of hydration. The dark blue curve represents the seed in storage condition.

Source: Provided by Éverton Lucas de Oliveira.

Also, during the period of the imbibition of the seed, both peaks associated to the water content shows a little difference of the values between the initial and final period, which can represent that the water absorbed has a more restrict mobile condition, and it is possible to observe just the increase in amplitude related to the water absorption.

The first graph on Figure 33 shows the evolution of the spin-spin relaxation time T_2 during the 6 hours of imbibition of a single seed with low vigor lot. As the same behavior of the seed with high vigor, seeds with low vigor also display an increased amplitude in the shortest peak on the curve, but with a greater displacement compared to the previous case, which may be due to a disorder on the membranes of the seed tissue which allows a higher water absorption rate.

In the second graph in Figure 33, it is shown the evolution of a distribution of the spin-lattice relaxation time T_1 during the time of the imbibition of the seed. Also, as the same behavior of the transverse relaxation time, the longitudinal relaxation time shows a more pronounced shift with the direction of the longest relaxation times compared to a seed with high vigor.

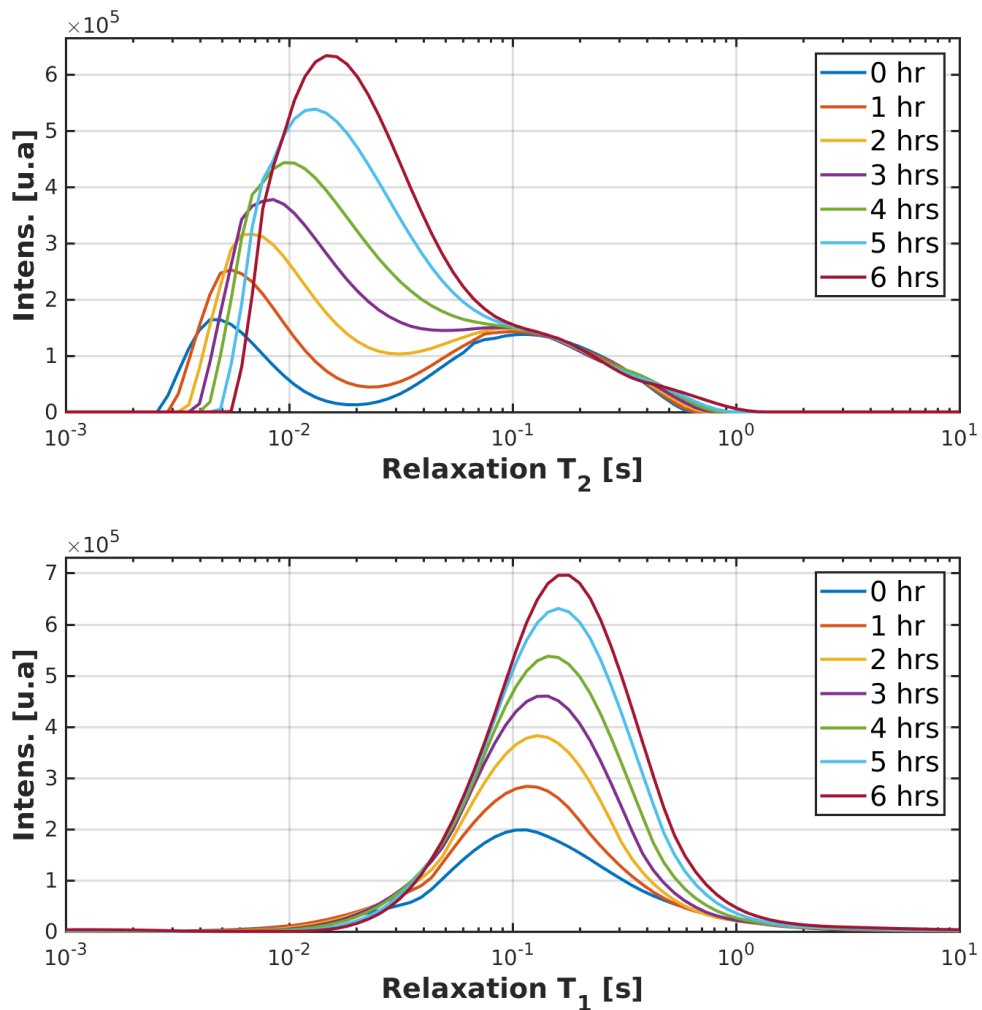


Figure 33 – Relaxation time curves for both T_2 and T_1 obtained by Inverse Laplace Transformation (ILT) for a single seed with low vigor during 6 hours of hydration. The dark blue curve represents the seed in storage condition.

Source: Provided by Éverton Lucas de Oliveira.

Also, other interesting results are the amplitudes of the water peak for transverse and longitudinal relaxation times in both cases. The water peak for T_2 is bigger, as the water peak for T_1 is twice greater in seeds with low vigor than seeds with high vigor, showing that seeds with low vigor could be more affected by the

disorganized cell structure in the seed membrane system, as discussed by Krishnan, P., et. al.⁸³

5 CONCLUSIONS

Although all the complexity of an MRI scanner, the RF coil is a primary element of fundamental importance for obtaining images. Thus, the development of a solenoid coil dedicated to the dimensions of the seed for the acquisition of images brought significant results, since there was a great increase in the SNR ratio, through the improvement of the fill factor. In this work the coil works as a transceiver, which means that it be able to transmit power with homogeneous RF field and to receive the signal of the sample with high sensitivity.

MRI is one of the most important imaging techniques due to its versatility in obtaining the most various types of contrast, as well as one of the safest techniques, as it does not use ionizing radiation, it is non-invasive and non-destructive. Thus, the optimization of the parameters in the MR images of the FLASH and ZTE sequences brought a fantastic increase in resolution and contrast of the internal tissues in the seeds, although the acquisition time was sacrificed.

The FLASH image, despite the echo time of 3 ms, that results in a lost of part of the MR signal, was useful to observe structures of the soybean seed, due to its longest relaxation times of the internal tissues compared to corn seeds. The gradient of brightness in a radial manner reflects the hydration of the seed tissues due to the contact to the paper towel. The damages cause by chinch bug bites result in regions inside the seed with absence of signal, due to the deterioration of internal tissues. On the other hand, immature seeds show internal tissues as the same aspects than to healthy seeds, although the region of the embryonic axis present malformations.

The ZTE image shows clearly the hard region of the corn seed (endosperm), the region of the shortest relaxation times, as expected due to the absence of signal when the image of the corn seed was acquired with the FLASH sequence. Moreover, due the differences of the relaxation times of the regions of the endosperm and embryo, the ZTE image present a good contrast, show the region that produce more signal is more brightness compared to the other region that produce less signal. It was also possible to observe the wormholes caused by the damage of a weevil develop inside the seed.

Also, for the first time, this work shows with success a propose of modification of the ZTE sequence applied in combination with the contrast technique named Magnetization Transfer. In corn seed, the MT suppress the signal of the region of the

endosperm, but with a little brightness of the aleurone layer, confirm that this region has the shortest relaxation times compared to the region of the embryo. In soybean seed, it is possible to visualize the specialized tissues for metabolic transportation inside the region of the cotyledons without the necessity of hydration and, that these tissues have longest relaxation times when compared to other regions of the cotyledons.

Some improvements can be made in the MT-ZTE sequence to achieve better results, such as replacing a single pulse with a pulse train for more effective saturation of a given region within the object of study. The image of the soybean seed was acquired with just two averages, so the aspect of that image could be improved increasing the number of averages.

The relaxometry results shows clearly the differences between a soybean seeds with high and low vigor. While in the high vigor seeds the changes in both longitudinal and transverse relaxation times are shorter, in the low vigor seeds the changes are bigger, also in relation to the amplitude, resulting in a more absorption of water in seeds with low vigor than with high vigor up to 6 hours of the imbibition process. These results could reflect the higher disorganization of the external membranes in seeds with low vigor.

Future studies can be conducted utilizing friendly contrast agents in the MR images to monitoring the absorption of water and the flow inside the tissues of the seeds with times longer than the phase I of germination (imbibition). Preliminary studies with gadolinium have not produced satisfactory results and have not been presented.

Also, the MT-ZTE purposed here as a modified sequence could be utilized in other biological or non-biological systems that present short relaxation times behavior, and the MT could work as a filter of the shortest ones. Furthermore, the MT pulse could be tested for other displacement to observe the changes that are produced.

REFERENCES

- 1 CARVALHO, M. **Mercado de sementes fatura R\$20 bi no país, mas tem prejuízo bilionário com pirataria e desrespeito à propriedade intelectual.** 2020. Available from: <https://www.noticiasagricolas.com.br/videos/agronegocio/263974-mercado-de-sementes-fatura-r20-bi-no-pais-mas-tem-prejuizo-bilionario-com-pirataria-e-desrespeito-a.html#.YGyiJOhKgUH>. Accessible at: 5 April 2021.
- 2 FRANÇA NETO, J. B.; HENNING, A. A. **Qualidade fisiológica e sanitária de sementes de soja.** Londrina: EMBRAPA-CNPSo. 1984.
- 3 CARVALHO, N. M.; NAKAGAWA, J. **Sementes: ciência, tecnologia e produção.** 4. ed. Jaboticabal: FUNEP, 2000.
- 4 BEWLEY, J. D. **Seeds: physiology of development and germination.** 2nd. ed. New York: Plenum Press, 1994.
- 5 PETERSON, J. M.; PERDOMO, J. A.; BURRIS, J. S. Influence of kernel position, mechanical damage and controlled deterioration on estimates of hybrid maize seed quality. **Seed Science and Technology**, v. 23, n. 3, p. 647-657, 1995. ISSN 0251-0952.
- 6 CICERO, S. M.; BANZATTO JUNIOR, H. L. Avaliação do relacionamento entre danos mecânicos e vigor, em sementes de milho, por meio da análise de imagens. **Revista Brasileira de Sementes**, v. 25, n. 1, p. 29-36, 2003. ISSN 1806-9975.
- 7 RUSSIN, J. S. *et al.* Within-plant distribution of, and partial compensation for, stink bug (Heteroptera: Pentatomidae) damage to soybean seeds. **Journal of Economic Entomology**, Louisiana, v. 80, p. 215-220, 1987. ISSN 0022-0493.
- 8 MILES, P. W. The saliva of hemiptera. **Advances in Insect Physiology**, Cambridge, v. 9, p. 183-255, 1972. ISSN 0065-2806.
- 9 PANIZZI, A. R.; NIVA, C. C.; HIROSE, E. Feeding preference by stink bugs (Heteroptera: pentatomidae) for seeds within soybean pods. **Journal of Entomological Science**, Tifton, v. 30, p. 333-341, 1995. ISSN 0749-8004.
- 10 SINCLAIR, J. B.; BACKMAN, P. A. **Compendium of soybean diseases.** 3rd. ed. St. Paul: The American Phytopathological Society, 1989. 106 p.
- 11 VILLAS BÔAS, G. L. *et al.* **Efeito de diferentes populações de percevejos sobre o rendimento e seus componentes, características agronômicas e qualidade de semente de soja.** Londrina: EMBRAPA-CNPSo. 1990. p. 43.
- 12 VILLAS BÔAS, G. L. *et al.* **Efeitos de cinco populações de percevejos sobre o rendimento e seus componentes, características agronômicas e qualidade de sementes de soja.** Londrina: EMBRAPA-CNPSo. 1982. p. 13.

- 13 FRANÇA-SILVA, F. *et al.* Radiographic analysis to test maize seeds for the presence of *Sitophilus zeamais* (Coleoptera: Curculionidae). **Seed Science and Technology**, v. 47, p. 249-260, 2019. ISSN 0251-0952.
- 14 FRANÇA-SILVA, F. *et al.* Determination of *Sitotroga cerealella* (Lepidoptera: Gelechiidae) infestation in wheat seeds by radiographic and multispectral image analysis. **Agronomy Journal**, v. 112, n. 5, p. 3695-3703, 2020. ISSN 0002-1962.
- 15 CICERO, S. M. *et al.* Evaluation of mechanical damages in seeds of maize (*Zea mays* L) by X ray and digital imaging. **Seed Science and Technology**, v. 26, n. 2, p. 603-612, 1998. ISSN 0251-0952.
- 16 OBANDO FLOR, E. P. *et al.* Avaliação de danos mecânicos em sementes de soja por meio da análise de imagens. **Revista Brasileira de Sementes**, v. 26, n. 1, p. 68-76, 2004. ISSN 1806-9975.
- 17 PINTO, T. L. F. *et al.* An assessment of mechanical and stink bug damage in soybean seed using X ray analysis test. **Seed Science and Technology**, v. 37, n. 1, p. 110-120, 2009. ISSN 0251-0952.
- 18 GOMES JUNIOR, F. G.; CICERO, S. M. X-ray analysis to assess mechanical damage in sweet corn seeds. **Revista Brasileira de Sementes**, v. 34, n. 1, p. 78-85, 2012. ISSN 1806-9975.
- 19 MONDO, V. H. V.; CICERO, S. M. Análise de imagens na avaliação da qualidade de sementes de milho localizadas em diferentes posições na espiga. **Revista Brasileira de Sementes**, v. 27, n. 1, p. 9-18, 2005. ISSN 1806-9975.
- 20 PUPIM, T. L. *et al.* Adequação do teste de raios X para avaliação da qualidade de sementes de Embaúba. **Revista Brasileira de Sementes**, v. 30, n. 2, p. 28-32, 2008. ISSN 0101-3122.
- 21 FORTI, V. A.; CICERO, S. M.; PINTO, T. L. F. Avaliação da evolução de danos por "umidade" e redução do vigor em sementes de soja, cultivar TMG113-RR, durante o armazenamento, utilizando imagens de raios X e testes de potencial fisiológico. **Revista Brasileira de Sementes**, v. 32, n. 3, p. 123-133, 2010. ISSN 0101-3122.
- 22 GOMES-JUNIOR, F. G. *et al.* X-ray microtomography in comparison to radiographic analysis of mechanically damaged maize seeds and its effect on seed germination. **Acta Scientiarum Agronomy**, v. 41, n. 1, p. e42608, 2018. ISSN 1807-8621.
- 23 PLEWES, D. B.; KUCHARCZYK, W. Physics of MRI: a primer. **Journal of Magnetic Resonance Imaging**, v. 35, n. 5, p. 1038-1054, 2012. ISSN 1053-1807.
- 24 TANNÚS, A. *et al.* NMR imaging at IFQSC. **Medical Physics**, v. 15, n. 5, p. 801-801, 1988. ISSN 0094-2405.
- 25 SLICHTER, C. P. **Principles of magnetic resonance**. New York: Springer-Verlag, 1989.

- 26 HAACKE, E. M. *et al.* **Magnetic resonance imaging: physical principles and sequence design.** New York: Wiley-Liss, 1999.
- 27 REIF, F. **Fundamentals of statistical and thermal physics.** New York: McGraw-Hill, 1965.
- 28 ABRAGAM, A. **The principles of nuclear magnetism.** Oxford: Oxford University Press, 1961.
- 29 HANSON, L. G. Is quantum mechanics necessary for understanding magnetic resonance? **Concepts in Magnetic Resonance Part A**, v. 32A, n. 5, p. 329-340, 2008. ISSN 1546-6086.
- 30 ELSTER, A. D.; BURDETTE, J. H. **Questions and answers in magnetic resonance imaging.** 2nd ed. St Louis: Mosby, 2001.
- 31 RABI, I. I.; RAMSEY, N. F.; SCHWINGER, J. Use of rotating coordinates in magnetic resonance problems. **Reviews of Modern Physics**, v. 26, n. 2, p. 167-171, 1954. ISSN 1539-0756.
- 32 REDFIELD, A. G. Nuclear magnetic resonance saturation and rotary saturation in solids. **Physical Review**, v. 98, p. 1787-1809, 1955. ISSN 1536-6065.
- 33 WANG, J. *et al.* Factors influencing flip angle mapping in MRI: Rf pulse shape, slice-select gradients, off-resonance excitation, and B_0 inhomogeneities. **Magnetic Resonance in Medicine**, v. 56, p. 463-468, 2006. ISSN 1522-2594.
- 34 LEVITT, M. H. **Spin dynamics: basics of nuclear magnetic resonance.** 2nd ed. UK: Chichester, 2012.
- 35 HAHN, E. L. Nuclear induction due to free Larmor precession. **Physical Review**, v. 77, n. 2, p. 297-298, 1950. ISSN 1536-6065.
- 36 BLOEMBERGEN, N.; PURCELL, E. M.; POUND, R. V. Relaxation effects in nuclear magnetic resonance absorption. **Physical Review**, v. 73, n. 7, p. 679-712, 1948. ISSN 1536-6065.
- 37 BLOEMBERGEN, N. Spin relaxation processes in a two-proton system. **Physical Review**, v. 104, n. 6, p. 1542-1547, 1956. ISSN 1536-6065.
- 38 SOLOMON, I. Relaxation processes in a system of two spins. **Physical Review**, v. 99, n. 2, p. 559-565, 1955. ISSN 1536-6065.
- 39 GOLDMAN, M. Formal theory of spin-lattice relaxation. **Journal of Magnetic Resonance**, v. 149, n. 2, p. 160-187, 2001. ISSN 1090-7807.
- 40 HAHN, E. L. Spin Echoes. **Physical Review**, v. 80, n. 4, p. 580-594, 1950. ISSN 1536-6065.
- 41 FOERSTER, B. U. **Técnicas de aquisição rápida em tomografia por ressonância magnética nuclear.** 1994. 129 p. Dissertação (Mestrado em Física Aplicada) - Instituto de Física e Química de São Carlos, Universidade de São Paulo. São Carlos, 1994. DOI:10.11606/D.54.1994.tde-06122013-143859.

- 42 PAIVA, F. F. **Metodologia de imagens de NMR que utiliza um único pulso adiabático de inversão**. 2004. 116 p. Dissertação (Mestrado em Física Aplicada) - Instituto de Física de São Carlos, Universidade de São Paulo. São Carlos, 2004. DOI:10.11606/D.76.2004.tde-28042004-184322.
- 43 BRIGHAM, E. O. **The fast fourier transform**. United States: Prentice-Hall, 1974.
- 44 PAPOTI, D. **Transdutores de RF para experimentos de imagens em pequenos animais**. 2006. 144 p. Dissertação (Mestrado em Física Aplicada) - Instituto de Física de São Carlos, Universidade de São Paulo. São Carlos, 2006. DOI:10.11606/D.76.2006.tde-13092007-144440.
- 45 MANSFIELD, P.; MORRIS, P. G. **NMR imaging in biomedicine**. New York: Academic Press, 1982.
- 46 TWIEG, D. B. The k-trajectory formulation of the NMR imaging process with applications in analysis and synthesis of imaging methods. **Medical Physics**, v. 10, n. 5, p. 610-621, 1983. ISSN 0094-2405.
- 47 MEZRICH, R. A. A perspective on K-space. **Radiology**, v. 195, n. 2, p. 297-315, 1995. ISSN 1527-1315.
- 48 PIPE, J. G. Motion correction with PROPELLER MRI: application to head motion and free-breathing cardiac imaging. **Magnetic Resonance in Medicine**, v. 42, n. 5, p. 963-969, 1999. ISSN 0740-3194.
- 49 DIETRICH, T. J. *et al.* PROPELLER technique to improve image quality of MRI of the shoulder. **American Journal of Roentgenology**, v. 197, n. 6, p. 1093-1100, 2011. ISSN 0361-803X.
- 50 HAASE, A. *et al.* FLASH imaging: rapid NMR imaging using low flip-angle pulses. **Journal of Magnetic Resonance**, v. 67, n. 2, p. 258-266, 1986. ISSN 0022-2364.
- 51 ELSTER, A. D. Gradient-echo MR imaging: techniques and acronyms. **Radiology**, v. 186, n. 1, p. 1-8, 1993. ISSN 1527-1315.
- 52 WINKLER, M. L. *et al.* Characteristics of partial flip angle and gradient reversal MR imaging. **Radiology**, v. 166, n. 1, p. 17-26, 1988. ISSN 1527-1315.
- 53 WANG, D. *et al.* Inherent insensitivity to RF inhomogeneity in FLASH imaging. **Magnetic Resonance in Medicine**, v. 52, n. 4, p. 927-931, 2004. ISSN 0740-3194.
- 54 YOUNG, I. R.; BRYANT, D. J.; PAYNE, J. A. Variations in slice shape and absorption as artifacts in the determination of tissue parameters in NMR imaging. **Magnetic Resonance in Medicine**, v. 2, n. 4, p. 355-389, 1985. ISSN 0740-3194.
- 55 HAASE, A. Principles and applications of FLASH NMR imaging. **Magnetic Resonance Materials in Physics, Biology and Medicine**, v. 2, n. 3, p. 157-160, 1994. ISSN 1352-8661.
- 56 WEIGER, M.; PRUESSMANN, K. P. MRI with zero echo time. **eMagRes**, v. 1, n. 2, 2012. ISSN 2055-6101.

- 57 WEIGER, M.; PRUESSMANN, K. P.; HENNEL, F. MRI with zero echo time: hard versus sweep pulse excitation. **Magnetic Resonance in Medicine**, v. 66, n. 2, p. 379-389, 2011. ISSN 0740-3194.
- 58 WEIGER, M. *et al.* Exploring the bandwidth limits of ZTE imaging: spatial response, out-of-band signals, and noise propagation. **Magnetic Resonance in Medicine**, v. 74, n. 5, p. 1236-1247, 2015. ISSN 0740-3194.
- 59 WOLFF, S. D.; BALABAN, R. S. Magnetization transfer contrast (MTC) and tissue water proton relaxation in vivo. **Magnetic Resonance in Medicine**, v. 10, n. 1, p. 135-144, 1989. ISSN 0740-3194.
- 60 KNUTSSON, L. *et al.* CEST, ASL, and magnetization transfer contrast: how similar pulse sequences detect different phenomena. **Magnetic Resonance in Medicine**, v. 80, n. 4, p. 1320-1340, 2018. ISSN 0740-3194.
- 61 HENKELMAN, R. M.; STANISZ, G. J.; GRAHAM, S. J. Magnetization transfer in MRI: a review. **NMR in Biomedicine**, v. 14, n. 2, p. 57-64, 2001. ISSN 1099-1492.
- 62 LIMA, C. C. A.; SILVA, L. J.; CASTRO, W. S. **Apostila de morfologia externa vegetal**. 2006. (Anatomia vegetal). Available from: <http://www.anatomiavegetal.ib.ufu.br/pdfrecursosdidaticos/morfvegetalorgaSEMENTE.pdf>. Accessible at: 10 April 2021.
- 63 POPINIGIS, F. **Fisiologia da semente**. 2. ed. Brasília: AGIPLAN, 1977.
- 64 OLIVEIRA, L. E. M. **Morfologia de sementes**. 2015. (Temas em Fisiologia vegetal). Available from: <http://www.ledson.ufla.br/metabolismo-da-germinacao/morfologia-de-sementes/>. Accessible at: 10 April 2021.
- 65 MAYER, A. M.; POLJAKOFF-MAYBER, A. **The germination of seeds**. 3rd ed. Great Britain: Pergamon, 1982.
- 66 COSTA, J. G. C. Agência Embrapa de Informação Tecnológica. **Semente** Available from: [https://www.agencia.cnptia.embrapa.br/gestor/feijao/arvore/CONTAG01_9_1311200215101.html#:~:text=Ag%C3%AAncia%20Embrapa%20de%20Informa%C3%A7%C3%A3o%20Tecnol%C3%B3gica%20%2D%20Morfologia&text=A%20parte%20externa%20\(Figura%201,a%20semente%20com%20a%20placenta](https://www.agencia.cnptia.embrapa.br/gestor/feijao/arvore/CONTAG01_9_1311200215101.html#:~:text=Ag%C3%AAncia%20Embrapa%20de%20Informa%C3%A7%C3%A3o%20Tecnol%C3%B3gica%20%2D%20Morfologia&text=A%20parte%20externa%20(Figura%201,a%20semente%20com%20a%20placenta). Accessible at: 10 April 2021.
- 67 SNARR, J. E.; VAN AS, H. Probing water compartments and membrane permeability in plant cells by ^1H NMR relaxation measurements. **Biophysical Journal**, v. 63, n. 6, p. 1654-1658, 1992. ISSN 1542-0086.
- 68 ROCCULI, P. *et al.* Role of water state and mobility on the antiplasticization of green and roasted coffee beans. **Journal of Agricultural and Food Chemistry**, v. 59, n. 15, p. 8265-8271, 2011. ISSN 1520-5118.
- 69 FUKUOKA, M. *et al.* Moisture diffusion in a dry soybean seed measured using pulsed-field-gradient NMR. **Journal of Food Engineering**, v. 23, n. 4, p. 533-541, 1994. ISSN 0260-8774.

70 ISHIDA, N. *et al.* Analysis of physical states of water in soybean seeds by NMR. **Agricultural and Biological Chemistry**, v. 52, n. 11, p. 2777-2781, 1988. ISSN 0002-1369.

71 KRISHNAN, P.; NAGARAJAN, S.; DADLANI, M. M. A. V. Characterization of wheat (*triticum aestivum*) and soybean (*Glycine max*) seeds under accelerated ageing conditions by proton nuclear magnetic spectroscopy. **Seed Science and Technology**, v. 31, n. 3, p. 541-550, 2003. ISSN 1819-5717.

72 KRISHNAN, P. *et al.* Changes in seed water status as characterized by NMR in developing soybean seed grown under moisture stress conditions. **Biochemical and Biophysical Research Communications**, v. 444, n. 4, p. 485-491, 2014. ISSN 0006-291X.

73 RATKOVIC, S. Proton NMR of maize seed water: the relationship between spin-lattice relaxation time and water content. **Seed Science and Technology**, v. 15, n. 1, p. 147-154, 1987. ISSN 1819-5717.

74 QUIQUAMPOIX, H. *et al.* ^1H and ^{31}P NMR investigation of Gadolinium uptake in maize roots. **Journal of Inorganic Biochemistry**, v. 38, n. 4, p. 265-275, 1990. ISSN 0162-0134.

75 BACIC, G.; RATKOVIC, S. Water exchange in plant tissue studied by proton NMR in the presence of paramagnetic centers. **Biophysical Journal**, v. 45, n. 4, p. 767-776, 1984. ISSN 0006-3495.

76 KOIZUMI, M.; ISHIDA, N.; KANO, H. Location of sucrose and oils in a maize seed by NMR microscopy. **Bioscience, Biotechnology, and Biochemistry**, v. 59, n. 12, p. 2321-2323, 1995. ISSN 1347-6947.

77 ALEXANDER, D. E. *et al.* Analysis of oil content of maize by wide-line NMR. **Journal of the American Oil Chemists' Society**, v. 44, n. 10, p. 555-558, 1967. ISSN 0003-021X.

78 MONTRAZI, E. T. *et al.* Simultaneous acquisition for T_2 - T_2 exchange and T_1 - T_2 correlation NMR experiments. **Journal of Magnetic Resonance**, v. 289, p. 63-71, 2018. ISSN 1090-7807.

79 MARCOS-FILHO, J. **Fisiologia de sementes de plantas cultivadas**. 2. ed. Londrina: Abrates. 2015. p. 660.

80 MARASSI, A. G. **Aplicação da imagem por ressonância magnética para avaliação de injúrias mecânicas e tecidos deteriorados em sementes**. 2015. 112 p. Dissertação (Mestrado em Física Aplicada) - Instituto de Física de São Carlos, Universidade de São Paulo. São Carlos, 2015. DOI: 10.11606/D.76.2016.tde-25042016-094254.

81 FRANÇA-NETO, J. B. **Soja esverdeada - soluções práticas para o problema do campo à UBS**. Available from: <https://www.abrates.org.br/noticia/soja-esverdeada-solucoes-praticas-para-o-problema-do-campo-a-ubs>. Accessible at: 10 April 2021.

82 CALUCCI, L.; FORTE, C.; GALLESCHI, L. ^1H magnetization transfer in hydrated gluten and flour: effects of wheat aging. **Biomacromolecules**, v. 5, n. 5, p. 1824-1831, 2004. ISSN 1526-4602.

83 KRISHNAN, P. *et al.* Characterization of germinating and non-viable soybean seeds by nuclear magnetic resonance (NMR) spectroscopy. **Seed Science Research**, v. 14, n. 4, p. 355-362, 2004. ISSN 1475-2735.